Supplementary Information for:

Monolithic perovskite/organic tandem solar cells based on an ultra-thin metal-like metal-oxide interconnect.

K. O. Brinkmann[a,b*‡], T. Becker[a,b*], F. Zimmermann[a,b], C. Kreusel[a,b], T. Gahlmann[a,b], M. Theisen[a,b], T. Haeger[a,b], S. Olthof[c], C. Tückmantel[a,b], M. Günster[a,b], T. Maschwitz[a,b], F. Göbelsmann[a,b], C. Koch[c], D. Hertel[c], P. Caprioglio[d], F. Peña-Camargo[d], L. Perdigon[d], A. Al-Ashouri[e], L. Merten[f], A. Hinderhofer[f], L. Gomell[g], S. Zhang[g], F. Schreiber[f], S. Albrecht[e], K. Meerholz[c], D. Neher[d], M. Stolterfoht[d] and T. Riedl[a,b ‡]

[a] Institute of Electronic Devices, University of Wuppertal, Rainer-Gruenter-Str. 21, 42119 Wuppertal, Germany

[b] Wuppertal Center for Smart Materials & Systems, University of Wuppertal, Rainer-Gruenter-Str. 21, 42119 Wuppertal, Germany

[c] Department of Chemistry, University of Cologne, Greinstrasse 4-6, 50939 Cologne, Germany

[d] Soft Matter Physics, University of Potsdam, Karl-Liebknecht-Str. 24-25, 14476 Potsdam, Germany

[e] Young Investigator Group - Perovskite Tandem Solar Cells, Helmholtz-Zentrum Berlin, Kekuléstr. 5, 12489 Berlin, Germany

[f] Institute of Applied Physics, University of Tübingen, Auf der Morgenstelle 10, 72076 Tübingen, Germany

[g] Max-Planck-Institut für Eisenforschung GmbH, Max-Planck-Str. 1, 40237 Düsseldorf, Germany

[‡]E-mail: t.riedl@uni-wuppertal.de, brinkmann@uni-wuppertal.de

*equal contribution

Methods

Materials synthesis and device preparation

Perovskite sub cell and interconnect:
All processing steps of each sub cell were either carried out in inert atmosphere or high vacuum without any inert breaks.
The layer sequence of the perovskite *p-i-n* sub-cell is glass/HEL/$FA_{0.8}Cs_{0.2}Pb(I_{0.5}Br_{0.5})_3$/$PC_{61}BM$/AZO-NP/ALD-$SnO_x$/ALD-$InO_x$/(Ag). As substrate we used ITO-coated glass (17 x 17 mm^2) with a photoresist patterned to define the active area of 3.14 mm². Tandem cells additionally were covered with an illumination mask reducing the active area to 1.74 mm² to match the certification procedure. After cleaning and a brief plasma treatment, PTAA (Sigma Aldrich, 1.35 mg/ml in toluene) or MeO-2PACz (TCI, 0.1 mM in ethanol) was spin-coated at 6000 rpm for 20 s with a ramp of 8 s and annealed at 100°C for 30 min. For perovskite thin-film preparation, PbI_2 (0,75 M, ultradry from Alpha Aesar), $PbBr_2$ (0.25 M, ultradry from Alpha Aesar), CsBr (0.2 M, ultra-dry from Alpha Aesar) and FABr (0.8 M, from Greatcell Solar) were dissolved in a 3:7 mixture of N-Methyl-pyrrolidone (NMP) and Dimethylformamide (DMF) and stirred for at least 3 h. In some layers an additional 20 mM PbI_2 and 10 mM $PbBr_2$ were added. Prior to spin-coating, 33 mM Thiourea (2.5 mg/ml, Sigma Aldrich – previously dissolved 100 mg/ml in DMF) was added to the precursor solution. The perovskite deposition was performed following a gas quenching procedure, as described in earlier work.[1] Briefly the solution was spin-coated at 3000 rpm for 120 s with a ramp of 10 s. About 15 s after the ramp was finished, a 7 bar nitrogen flow (filtered with 5.0 µm PTFE) was directed at the substrate to introduce a supersaturated intermediate phase. Subsequently, during a 20 min annealing step at 100 °C the final perovskite layer forms. PEAI (TCI, 1 mg/ml in isopropanol) was optionally spin-coated at 6000 rpm for 30 s with a ramp of 8 s followed by another annealing step of 10 min at 100 °C. The optimum $PC_{61}BM$ layer thickness (see Figures S41) has been found to be around ~ 100 nm for the following process parameters: $PC_{61}BM$ purchased from Ossila, 50 mg/ml in chlorobenzene, was spin-coated with 1000 rpm for 30 s and a ramp of 1 s. Aluminium doped zinc oxide nanoparticles (AZO-NP) were processed from a NP-dispersion (Avantama AG, N21x, 2.5 wt% in a mixture of alcohols) diluted with isopropanol (1:2) and

spin-coated at 4000 rpm for 20 s using a ramp of 6 s. Some AZO layers were subsequently annealed at 80 °C, 90 °C or 100 °C for 90 min. For ALD deposition the solar cells were transferred into a Beneq TFS-200 reactor without inert break. SnO_x layers were grown from tetrakis(dimethylamino)tin(IV) (TDMA-Sn, Strem) and water. The reactor temperature during the deposition was 80 °C, TDMA-Sn was kept in a hot source at 45 °C and water in a liquid source at room temperature. Directly thereafter, InO_x was grown on top of SnO_x from Cyclopentadienylindium (CpIn, Strem), oxygen (purity 99.999%) and water.[2] The reactor temperature was 80 °C, CpIn was kept in a hot source at 50 °C, water in a liquid source at room temperature.

Please note that even though our ALD processes are based on water as oxygen source, which one might intuitively suspect to be detrimental to the active perovskite material, a single dose of H_2O in low pressure ALD typically creates an environment equivalent to a maximum of 0.1% of relative humidity.[3] This is significantly lower than the large variety of conditions mentioned in the literature to degrade the perovskite.[4, 5]

Silver was thermally evaporated in high vacuum (10^{-7} bar).

Organic sub cell:

As hole extractor a 15 nm of MoO_3 was thermally evaporated in high vacuum (10^{-7} bar). To form the binary BHJ PM6 and Y6 (Solamer Materials, weight ratio 1:1.2) were dissolved in chloroform (polymer concentration 7 mg/ml) and stirred for 3 h at 50 °C. For ternary BHJ an extra of $PC_{61}BM$ (American Dye Source) was added yielding a weight ratio of 1:1.2:0.2. Five minutes prior to BHJ processing 0.5 vol% of 1-Chloronaphthalene (Sigma Aldrich) was added to the solution. Spin-coating was carried out dynamically (solution was dropped on the middle of the rotating substrate) at 2500 rpm for 60 s. A subsequent thermal annealing of 100°C was applied followed by thermal evaporation of 10 nm C_{60}, 5 nm of BCP, and 100 nm Ag. Optional 100 nm MgF_2 was evaporated on the glass side to optimize reflectivity of the substrate.

Materials and device characterization

J/V characteristics of solar cells were recorded outside the glovebox under a continuous flow of nitrogen using a Keithley 2400 source measurement unit (SMU) and a 300 W Newport solar simulator (model 91 160, AM1.5G, 100 mW cm^{-2}) calibrated with a certified IEC 60904-9 compliant Si reference cell (Rera Systems).

J-V characteristics were recorded with a scanning speed of 500 mV s^{-1}. Stabilized power output recording was performed by continuously tracking the maximum power point under AM 1.5 illumination. Stabilized V_{OC} was recorded by continuously recording voltage without current flow. Long term measurements were conducted by continuous MPP tracking in a N_2 purged chamber under the illumination of two high power LED light sources (NIR: Thorlabs M850LP1 and VIS: Prizmatics UHP-T-HCRI or Thorlabs MWWHLP1 with a 630 nm low pass filter) joined together by a dichroic mirror. If not stated otherwise, we set the intensity of the light source(s) to generate a J_{sc} comparable to AM 1.5G sunlight illumination. In the case of organic single junctions this was achieved by first tuning the intensity of the LED_{NIR} to match the J_{sc} to that of the tandem under AM1.5G illumination. Then the white LED_{VIS} was added to finally achieve a J_{sc} corresponding to that of the organic single junctions under AM1.5G illumination. For the perovskite single junctions only the white LED_{VIS} was used for illumination.

For EQE measurements a homebuilt setup containing a chopped tunable light source (LOT MSH 150) and a lock-in amplifier (NF electronic instruments 5610B) was used. Calibration was performed with a Thorlabs PM100D power meter with a S130VC sensor head. For the determination of the EQE of the tandem-cells a protocol was followed as published before.[6] The sub-cells were therefore characterized under accurate bias conditions, to emulate operation under AM1.5G illumination. A 780 nm and a 520 nm laser diode (RLDC780-2-3 & RLCW520F, Roithner LaserTechnik GmbH) were used as bias light sources for the narrow-gap and wide-gap sub-cell, respectively. Transmission spectra were obtained using the same tunable light source (not chopped) and power meter. The respective layers were deposited on quartz substrates. UV-vis was acquired with a Jasco V-670 spectrometer. LED spectra were determined using an Ocean Optics spectrometer (USB2000+XR1-ES).

Sheet resistance was determined from measurements following the van-der-Pauw geometry in a homebuilt setup using a Keithley 2400 SMU and Keithley 182 voltmeter. Charge carrier density was determined from Hall measurements using the same setup and a magnetic field of 0.75 T.

SEM images were obtained with a Phillips XL-30 SFEG. Atomic force microscopy was conducted with a Bruker Innova system. XRD characterization was conducted with Cu-$K\alpha_{1,2}$ source (Philips C'Pert Pro MPD). Ellipsometry data of the metal oxide layers was acquired with an J.A. Woollam M-2000V ellipsom

eter and fitted with a cauchy approximation. Optical simulations have been carried out using SETFOS (Fluxim AG, Swizerland). Details of the simulation can be found in supplementary note 2.

Photoelectron spectroscopy was performed in a custom-built ultra-high vacuum system, with a base pressure < 10^{-9} mbar. For the detection of the photoelectrons in the UPS and XPS measurements, a hemispherical energy analyzer was used (Specs Phoibos 100). The excitation for XPS was done via a non-monochromated MgKα source (from VG, hv = 1253.6 eV) and for UPS by a monochromatic He source (VUV500, VG Scienta, hv = 21.22 eV). IPES was performed using a Kimball electron source (ELG-2) and a solid-state bandpass filter (Omnivac IPES2000). The samples were transferred into the measurement system without air exposure and were measured within 2 days after preparation.
The program XPSPEAK Version 4.1. was used to fit the XPS spectra. For the fitting of the molybdenum XPS peaks, a Shirley background was subtracted. The parameter for full width half max (FWHM) and the Lorentzian to Gaussian ratio (L:G) were kept constant for all Mo peaks at 1.22 eV and 23, respectively. The distances between the peaks of the different Mo oxidation states were held constant with 0.82 eV between Mo^{5+} and Mo^{6+} and 0.8 eV between Mo^{4+} and Mo^{5+}. Regarding the additional Mo feature we observed (see Figure S28): in case of MoO_3 on top of SnO_x, the position was at 0.88 eV higher binding energy compared to the Mo^{6+} signal of MoO_3, while on InO_x this shift was 0.74 eV.

Temperature dependent J/V scans of the recombination layers were conducted with an all-in-one solar cell characterization system (PAIOS, Fluxim AG) connected to a temperature-controlled cryostat (Linkham). Temperature was varied from room temperature upward, down and back to room temperature to ensure reproducibility.

Excitation for the PL imaging measurements was performed with a 520 nm CW laser (Insaneware) through an optical fibre into an integrating sphere. The intensity of the laser was adjusted to a 1 sun equivalent intensity by illuminating a 1 cm^2-size perovskite solar cell under short-circuit and matching the current density to the J_{SC} under the sun simulator (e.g. ~16 mA/cm^2 at 100 $mWcm^{-2}$, or $1x10^{21}$ photons $m^{-2}s^{-1}$ for a perovskite cell with a bandgap of 1.85 eV). A second optical fiber was used from the output of the integrating sphere to an Andor SR393i-B spectrometer equipped with a silicon CCD camera (DU420A-BR-DD, iDus). The system was calibrated by using a halogen lamp with known spectral irradiance, which was shone into to integrating sphere. A spectral correction factor was established to match the spectral output of the detector to the calibrated spectral irradiance of the lamp. The spectral photon density was obtained from the

corrected detector signal (spectral irradiance) by division through the photon energy (hf), and the photon numbers of the excitation and emission were obtained from numerical integration using Matlab. In a last step, three fluorescent test samples with high specified PLQY (~70%) supplied from Hamamatsu Photonics were measured where the specified value could be accurately reproduced within a small relative error of less than 5%.

Grazing incidence wide angle X-ray scattering was performed on a xenocs XEUSS 2.0 laboratory beamline using Cu-K_α radiation. The incident angles were below 0.5°, while the pressure in the sample chamber during the experiment was 0.1 bar. XRR measurements were recorded with a GE XRD 3003 TT diffractometer in ambient environment, also using Cu-K_α radiation. Synchrotron GIWAXS measurements were done at beamline ID10 of the ESRF under nitrogen conditions. Beam energy was 22 keV, with incidence angles varying from 0-0.3°.

Scanning transmission electron microscopy (STEM) was performed on a Titan Themis microscope operated at 300 kV. Aberration corrected STEM probe has <1 Å size and a convergence semi-angle of 24 mrad. High angle annular dark field (HAADF) and annular bright field (ABF) images were acquired using collection angles of 73-200 and 8-16 mrad respectively. Cross-sectional sample for STEM was prepared by a Scios2 focused ion beam (FIB) with a C marker layer to protect the sample surface.[7]

Energy dispersive X-ray spectroscopy (EDS) spectrum imaging was collected by a SuperX detector. The elemental distribution within the ALD layers were examined by EDS spectrum imaging, as shown in Figure S22. It is noteworthy that In-L and Sn-L X-ray emission peaks overlap, so that the traditional quantification by integrating peak intensity over fixed windows leads to interference between the SnO_x / InO_x layers. Therefore, we applied multivariate statistical analysis to separate the X-ray emission signals from In and Sn. In this case, we used non-negative matrix factorization, an algorithm widely applied in microanalysis including spectrum imaging of EDS and electron energy loss spectroscopy.[8,9]

Supplementary Note 1. Quantification of the QFLS in partial cell stacks

To calculate the quasi-Fermi level splitting, we can use the Shockley-Queisser equation which links the radiative recombination density of free charges (J_{rad}) with the chemical potential per free electron-hole pair (μ) or the quasi-Fermi level splitting (QFLS) in the active material.[10, 11]

$$J_{\mathrm{rad}} = J_{0,\mathrm{rad}} \exp(\mu/k_{\mathrm{B}}T) \ , \qquad \text{(eq. 1)}$$

Here, $J_{0,\mathrm{rad}}$ is the radiative thermal recombination current density in the dark, k_{B} the Boltzmann constant and T the temperature. We note that equation 1 is a simplification of Würfel's generalized Planck law which is only valid for a QFLS that is a few $k_{\mathrm{B}}T$ smaller that the bandgap $\mu < E_{\mathrm{G}} - 3k_{\mathrm{B}}T$.[12] If radiative recombination comes only from free charges, the radiative recombination current is identical to the photoluminescene yield times the elementary charge, that is $J_{\mathrm{rad}} = \phi_{\mathrm{PL}} \cdot e$. Moreover, we can define the photoluminescence quantum yield (PLQY) as the ratio of radiative to total recombination ($J_{\mathrm{R,tot}}$), where the latter is identical to the generation current density (J_{G}) under open-circuit conditions (V_{OC})

$$\mathrm{PLQY} = \frac{J_{\mathrm{rad}}}{J_{\mathrm{R,tot}}} = \frac{J_{\mathrm{rad}}}{J_{\mathrm{G}}} \qquad \text{(eq. 2)}$$

Therefore, we can relate the QFLS to the measured PLQY in the following way

$$\mu = k_{\mathrm{B}}T \ln(\mathrm{PLQY} * \frac{J_{\mathrm{G}}}{J_{0,\mathrm{rad}}}) \qquad \text{(eq. 3)}$$

We also note that equations 2 and 3 are only valid if the spectral dependence of J_{rad} is identical to $J_{0,\mathrm{rad}}$, meaning recombination goes through the same channels regardless of the QFLS.

In order to quantify the intensity dependence of the QFLS, we consider the following points. Firstly, equation 3 shows that the QFLS depends on the temperature. We note that we have measured the temperature on the samples during the illumination at various light intensities using an infrared sensor. Even at an intensity of 5 equivalent suns, which is the upper limit for the results shown in the main text, we observe a negligible temperature increase on the sample (~1°C). We attribute this to the fast dissipation of heat from the rather small illumination spot area (1 cm^2) during the measurement.

Secondly, the generation current density J_{G} was approximated with the short-circuit current density of the complete solar cell. Similarly, the $J_{0,\mathrm{rad}}$ was estimated by integrating the overlap of the external quantum efficiency of the device (EQE) with the black body spectrum ϕ_{BB} at 300 K over the energy.

$$J_{0,\mathrm{rad}} = \int \mathrm{EQE}\, \phi_{\mathrm{BB}}\, d\epsilon \qquad \text{(eq. 4)}$$

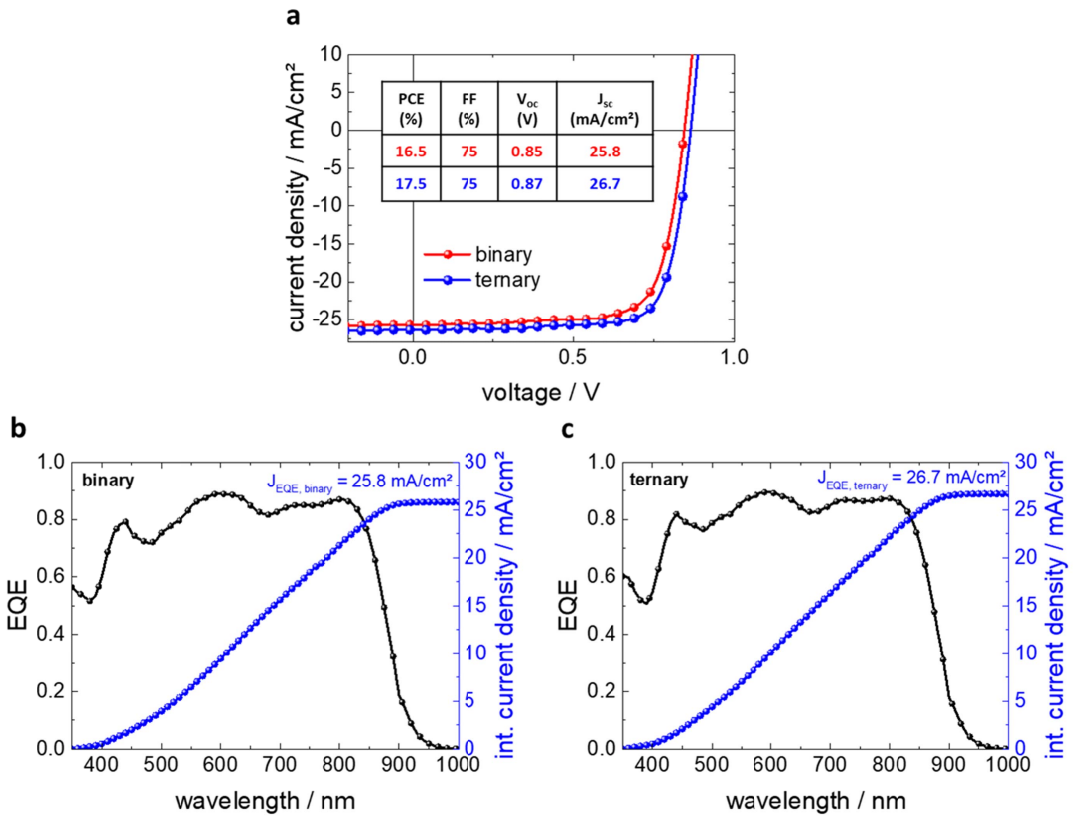

Figure S1: **a,** *J-V scans and respective cell parameters of champion binary and ternary OSCs and* **b,** *EQE as well as derived short circuit current density of a binary OSC and* **c,** *a ternary OSC.*

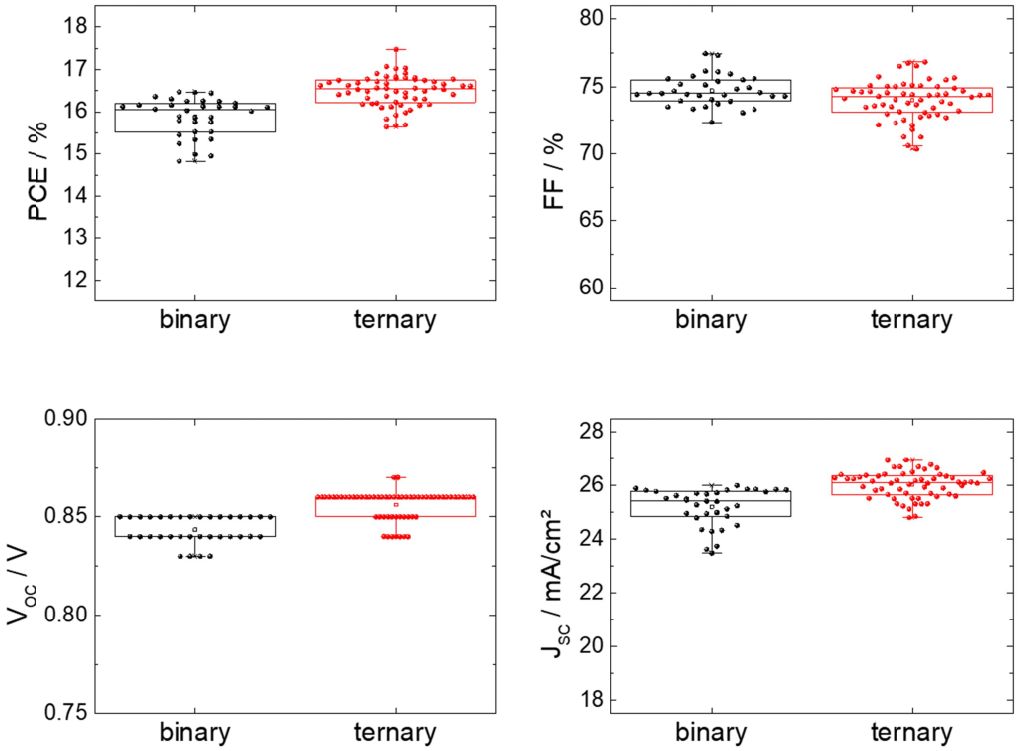

Figure S2: Statistics (box plot, 25% - 75% with mean line and data overlay) of 34 binary (PM6:Y6) and 60 ternary (PM6:Y6:$PC_{61}BM$) organic solar cells

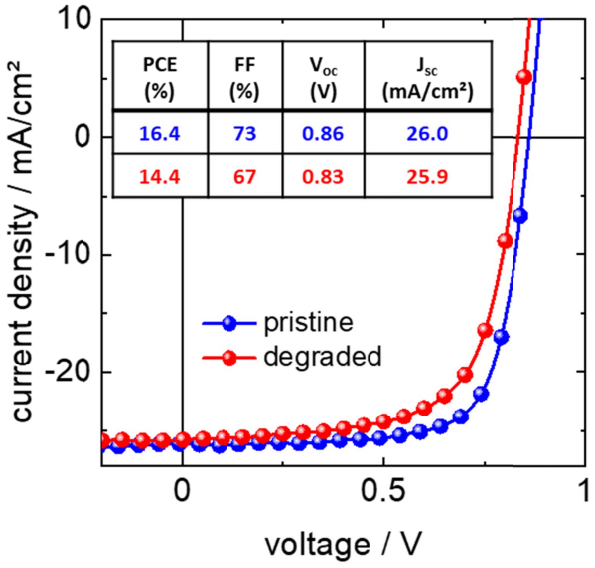

Figure S3: J/V of ternary OSCs before (pristine) and after 90h continuous illumination with LED_{VIS} + LED_{NIR}

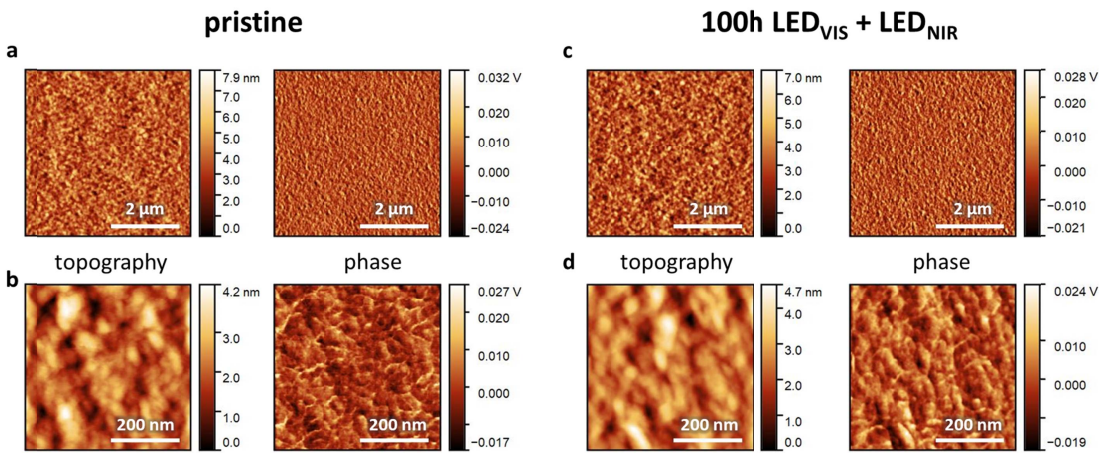

Figure S4: Results of atomic force microscopy (topography and phase images) of ternary (PM6:Y6:$PC_{61}BM$) bulk heterojunctions deposited on top of a silicon substrate ***a, b*** *pristine and* ***c, d*** *after stressing by illumination for 100 h (LED_{VIS} + LED_{NIR}). No obvious changes in the surface morphology can be identified after illumination stress.*

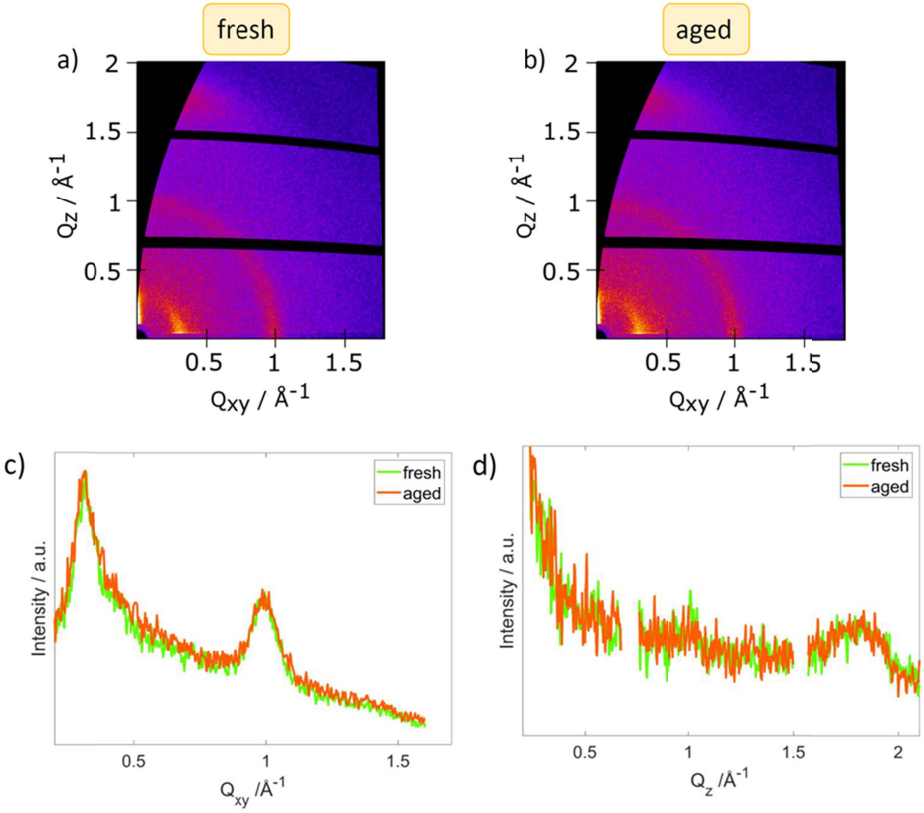

Figure S5: ***a,b,*** *Reciprocal space maps of fresh and aged (100 h LED_{VIS} + LED_{NIR}) ternary (PM6:Y6:$PC_{61}BM$) bulk heterojunctions obtained by grazing incidence wide angle scattering (GIWAXS)* ***c,*** *horizontal and* ***d,*** *vertical profiles of the reciprocal space maps showing no detectable sign for changes in the molecular order.*

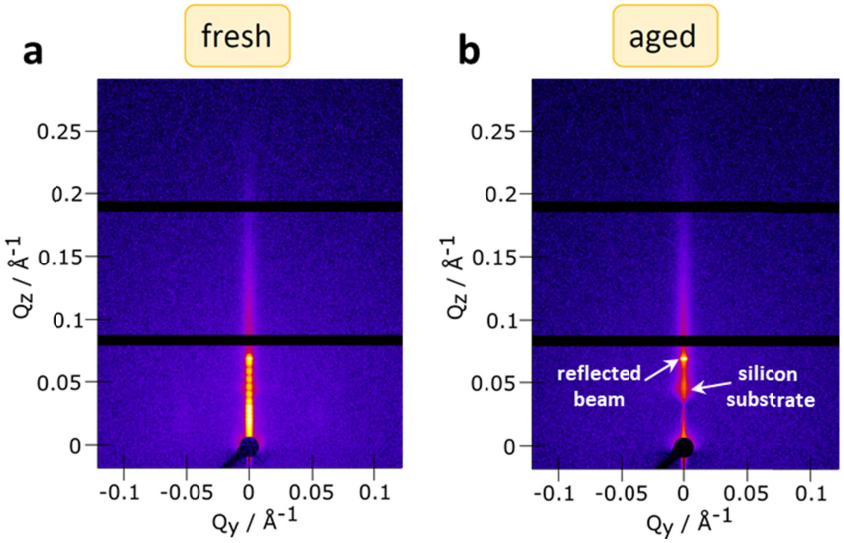

Figure S6: Grazing incidence small angle x-ray scattering (GISAXS) images of ***a,*** *fresh and* ***b,*** *aged ternary bulk heterojunctions deposited on top of a silicon substrate. The strong peak at around 0.07 Å^{-1} in Q_z corresponds to the reflection from the surface of the primary beam. A further signal, positioned at 0.045 Å^{-1} in Q_z for both samples corresponds to the total reflection edge of the silicon substrate (Yoneda wing). The disappearance of the out-of-plane oscillations as well as of very weak in-plane signals (at 0.05 Å^{-1}) in GISAXS might hint to slight changes in the correlations of surface domains. Overall, no clear indication of illumination induced ordering/packing (segregation) of the bulk heterojunction could be detected.*

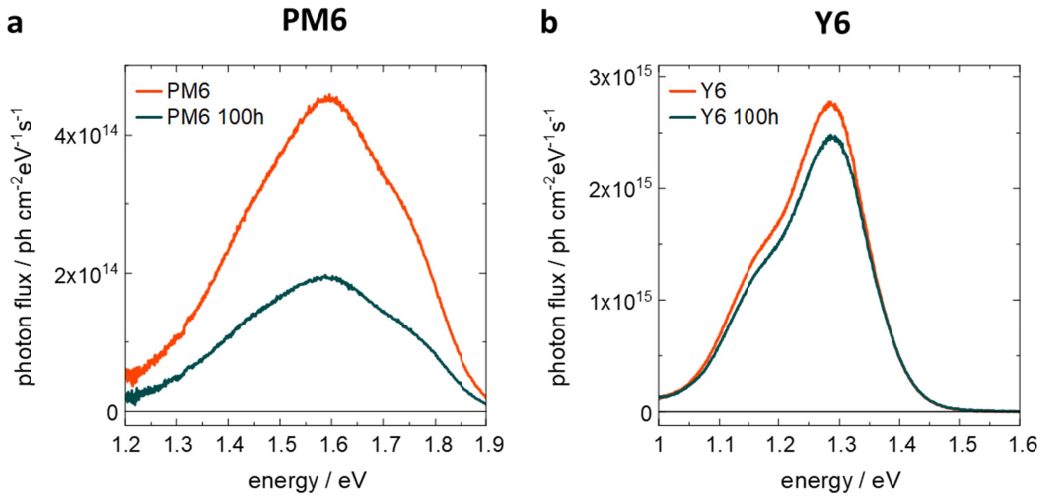

	PLQY (pristine)	PLQY (100h illum.)
PM6	3.0x10^{-3}	1.3x10^{-3}
Y6	1.7x10^{-2}	1.4x10^{-2}

Figure S7: Photon flux of photoluminescence for ***a,*** *PM6 and* ***b,*** *Y6 layers pristine and after 100 h illumination with both the white (LED$_{VIS}$) and near infrared (LED$_{NIR}$) LED (Figure 1c), as well as the corresponding photoluminescence quantum yield.*

Supplementary Note 2. Semi-empirical electro-optical simulation

As input data for the simulation the complex refractive indices (optical constants *n* & *k*) of all layers in the tandem stack are needed. For all layers except the perovskite and organic active layers the data was determined either by optical absorption or spectral ellipsometry measurements. To gather data for the perovskite and organic layers with different bandgap energies, a different approach has been used. At first the optical constants for known perovskite and organic absorbers were taken from literature.[13, 14] The data was then offset in wavelength to construct data for similar materials with varied energy gap.

To determine the J_{sc} of the respective tandem cells, a transfer matrix algorithm was then used to calculate the charge generation due to photon absorption inside the active layers upon illumination of the whole tandem stack with the AM1.5G spectrum. This is done for varying layer thicknesses up to 800 nm for the perovskite and up to 150 nm for the organic layer. Due to the chosen limits in layer thickness we can assume negligible transport losses inside the active layers and thus an internal quantum efficiency (IQE) of 100% for both sub-cells, which has also been reported to be reasonable.[15, 16] The charge generation in each active layer can be translated into a maximum possible current density ($J_{sc,max}$) of each sub-cell for each given thickness combination.

Describing the tandem device as a serial connection of both sub-cells, the sub-cell providing the lower $J_{sc,max}$ can be considered as current limiting for the entire device. As a result the maximum J_{sc} of the tandem device is obtained by determining the highest value of all minimal $J_{sc,max}$ values for each thickness combination.

As discussed in the main text, we assume a loss of 0.5 V in V_{oc} with respect to E_g/q for each sub-cell and a *FF* of the tandem of 80% as a consevative estimate. The results for the more optimistic scenario (FF = 85% and loss in V_{oc} compared to E_g/q of 0.4 V) can be seen in Figure S8.

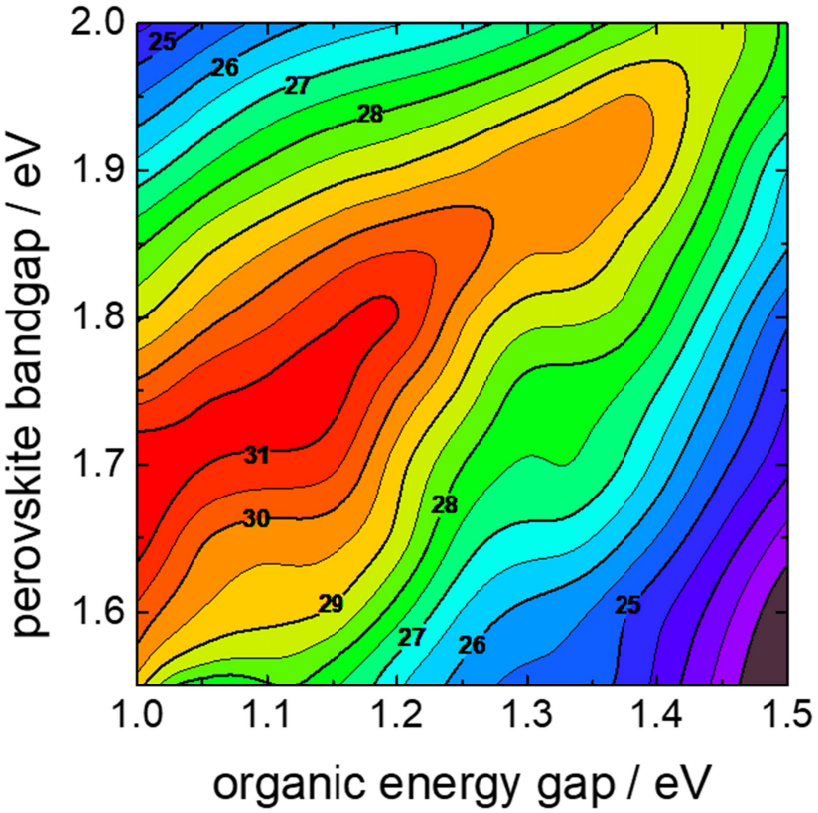

Figure S8: Semi-empirical model of the tandem cell efficiency vs. energy-gap of organic and perovskite sub-cells considering a more optimistic scenario with 0.4 V loss in V_{oc} compared to E_g/q in each cell and an overall FF of 85%.

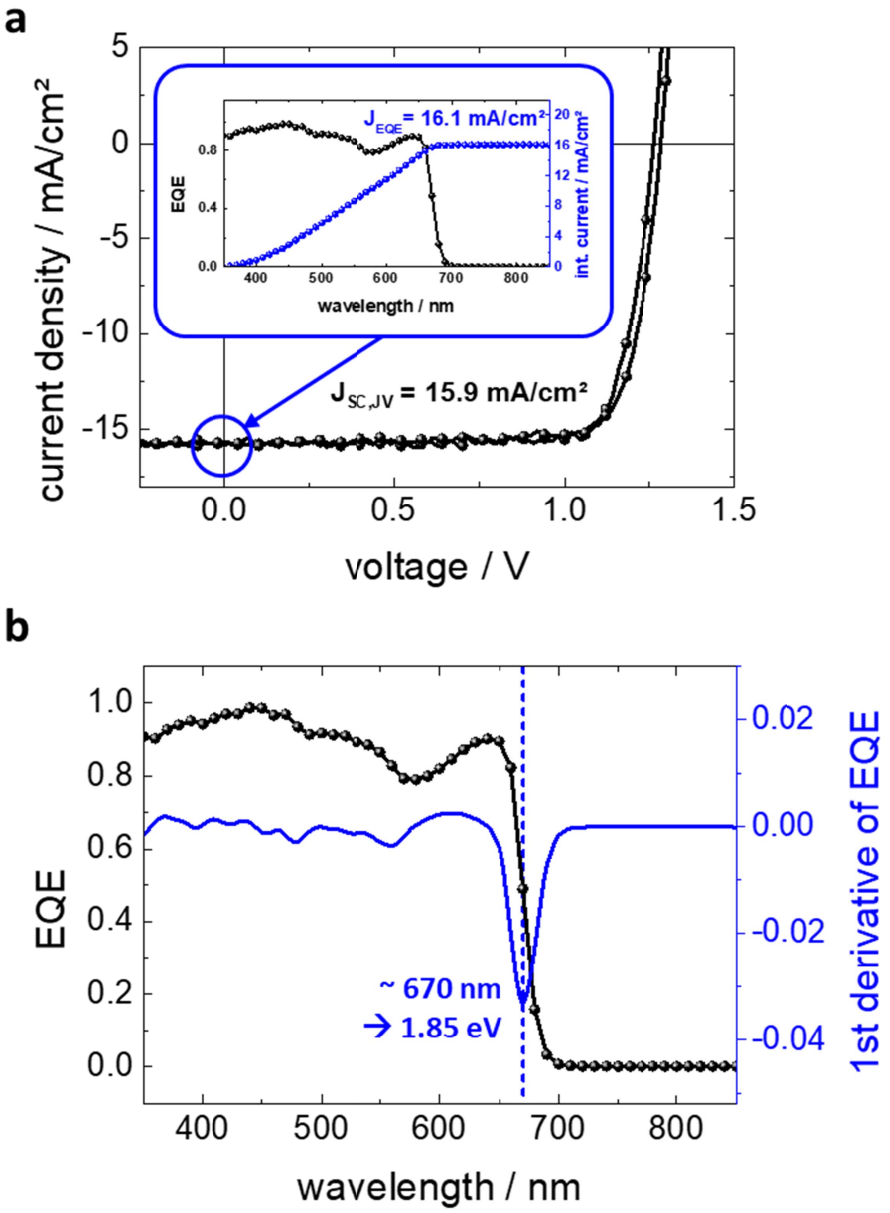

Figure S9: ***a,*** *J/V and EQE (inset) for a representative PSC (90°C annealing) and* ***b,*** *estimated bandgap by 1st derivative of the EQE spectrum.*[17]

Supplementary Note 3. Possible origin of the suppression of halide segregation

In recent work it was possible to map parasitic recombination by means of PL-intensity and link it to the tendency of a perovskite to segregate.[18]
It could be shown that segregated, low bandgap domains predominantly form at sites that initially show a low photoluminescence intensity. This correlation strongly indicates, that halide segregation is linked to charge trapping and concomitant parasitic recombination. Considering that we significantly decreased parasitic recombination by the introduction of MeO-2PACz as HEL, we believe that this might likewise be the origin of the reduced tendency of halide segregation. A somewhat similar observation was presented by Belisle et al., who reported reduced halide segregation upon topside defect passivation with trioctylphosphine oxide (TOPO) in their $MAPb(I_{0.66}Br_{0.33})_3$ layers.[19] Other passivation agents have also been reported to reduce halide segregation.[20]
To further analyze halide segregation in our MeO-2PACz/perovskite assembly we increased the duration of illumination up to 30 min. We found that halide segregation is indeed not entirely eliminated on this time scale, as some PL signal indicative for segregated perovskite occurs (Figure S11). As such, the proper use of suitable charge extraction layers, that afford reduced interfacial recombination, may be a key to at least slow down detrimental halide segregation.

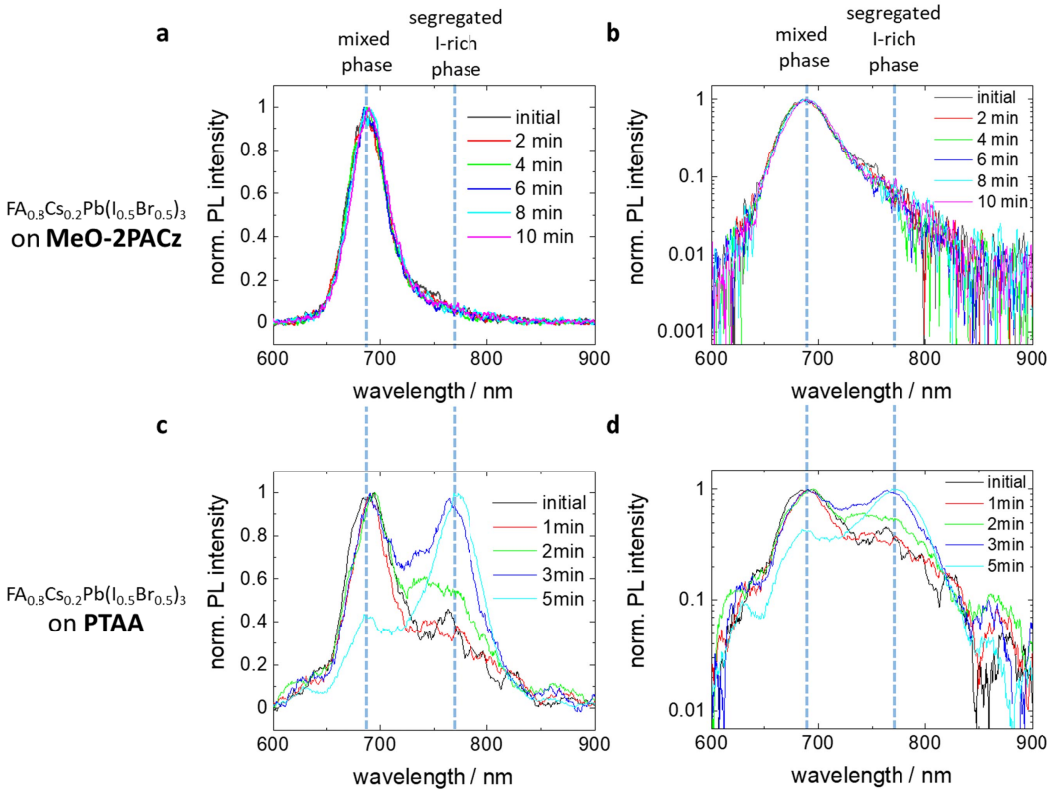

*Figure S10: Development of photoluminescence and continuous illumination of $FA_{0.8}Cs_{0.2}Pb(I_{0.5}Br_{0.5})_3$ on top of **a**, **b**, MeO-2PACz and **c**, **d**, PTAA in **a**, **c**, linear and **b**, **d**, logarithmic scale. The dashed lines indicate the photoluminescence maxima of the mixed and the segregated, iodine rich phase. Excitation was done with one sun equivalent.*

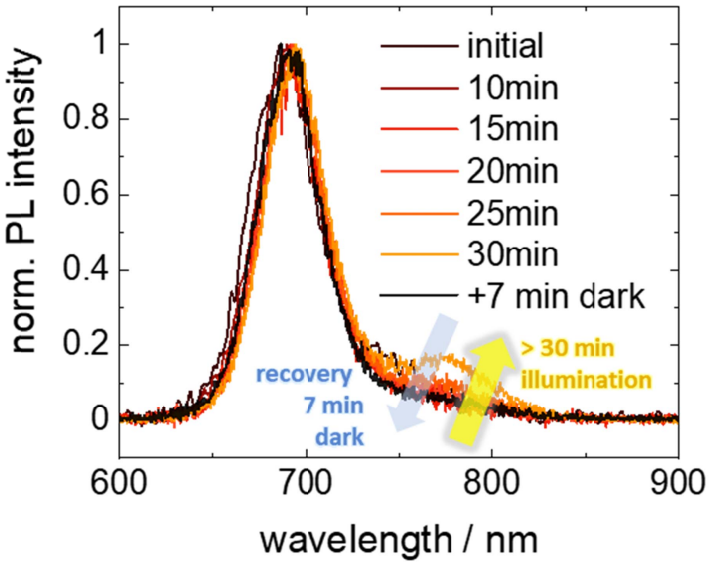

Figure S11: Evolution of photoluminescence under continuous illumination of $FA_{0.8}Cs_{0.2}Pb(I_{0.5}Br_{0.5})_3$ perovskite on top of MeO-2PACz over time, showing first signs of halide segregation after 30 minutes, followed by a 7 minutes period of darkness and a follow-up measurement evidencing the reversible nature of the effect.

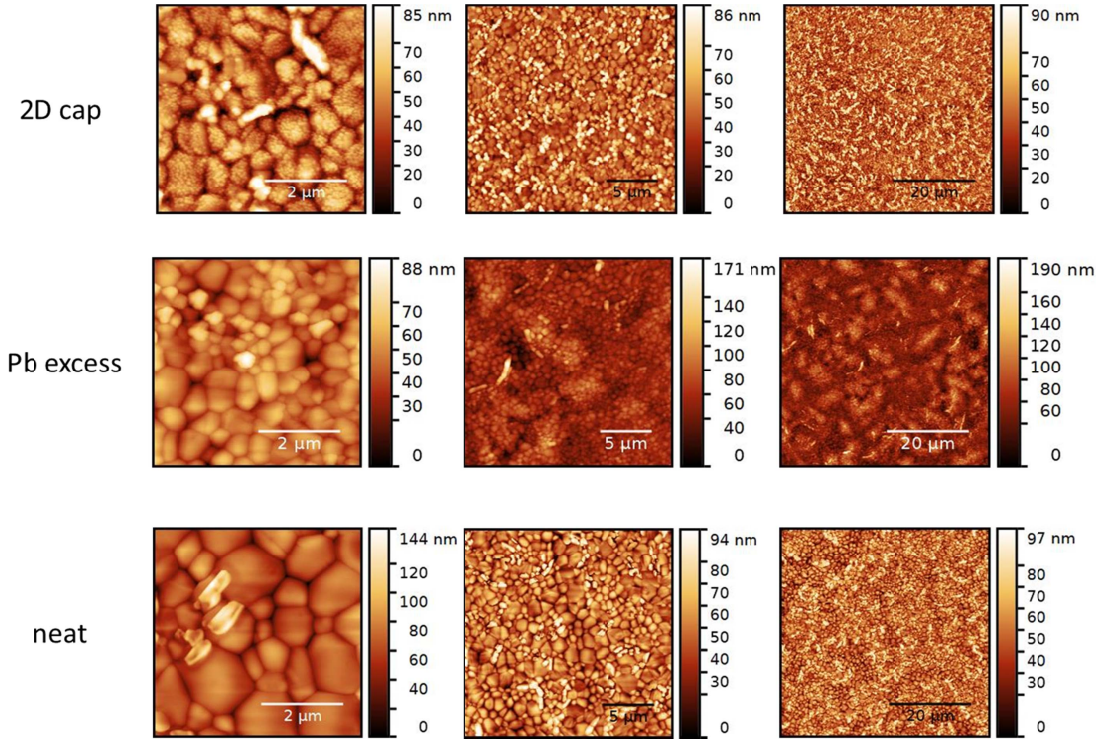

Figure S12: Topography measured by atomic force microscopy of perovskite layers w/o and with Pb excess and 2D cap passivation strategy.

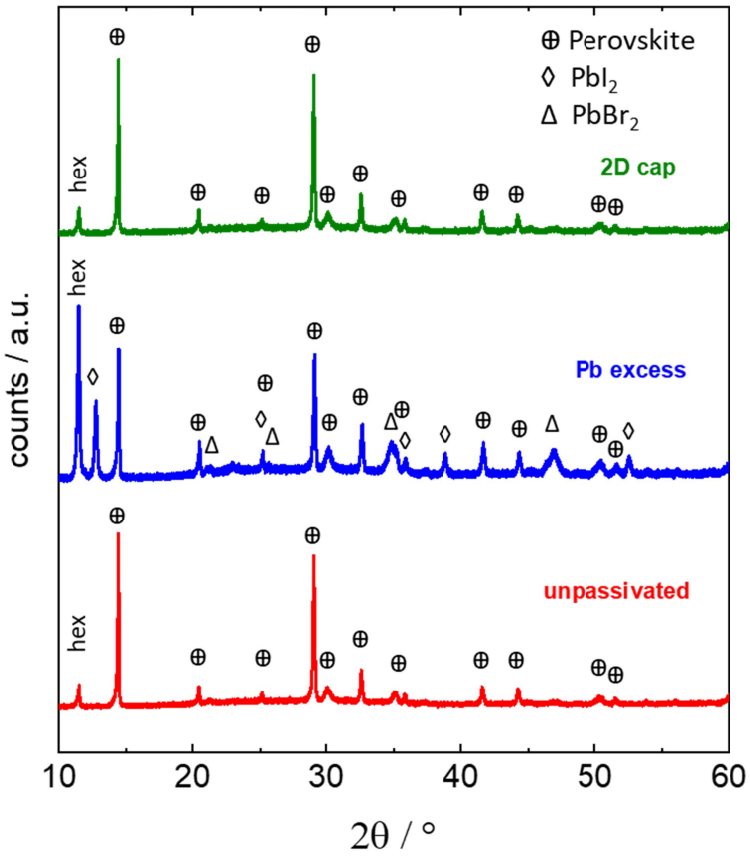

Figure S13: XRD diffractograms of perovskite layers w/o and with Pb excess and 2D cap passivation strategy. No noticeable difference is visible in XRD between unpassivated and 2D passivated samples. In Pb excess samples the diffraction peaks of PbI_2 and $PbBr_2$, both ingredients that were used in 2 mol % and 1 mol % excess respectively are clearly visible in addition to the other perovskite reflexes. Note that the reflection at 11.5° corresponds to a hexagonal crystal structure, as also visible in Figure S15. As confirmed in Figure S14, this reflection is not a result of degradation due to air exposure, but the hexagonal phase is most likely formed during the perovskite deposition process.

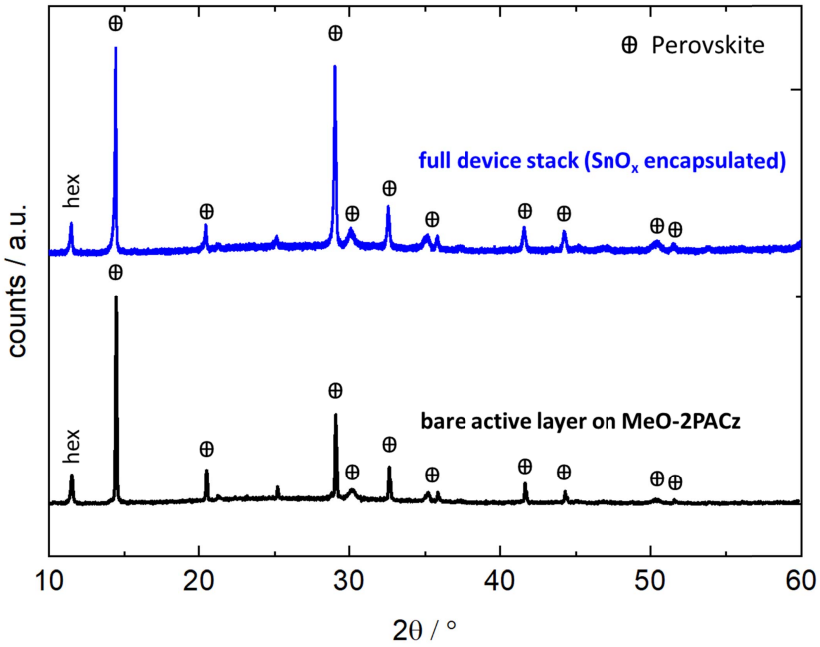

Figure S14: Direct comparison of x-ray diffractograms of a bare perovskite layer with that of a full device stack, which contains an ALD grown tin oxide permeation barrier that prevents the ingress of ambient air.[21] The reflection corresponding to the hexagonal (delta) phase is found in both samples, which confirms that the presence of hexagonal phase is not a result of degradation due to air exposure.

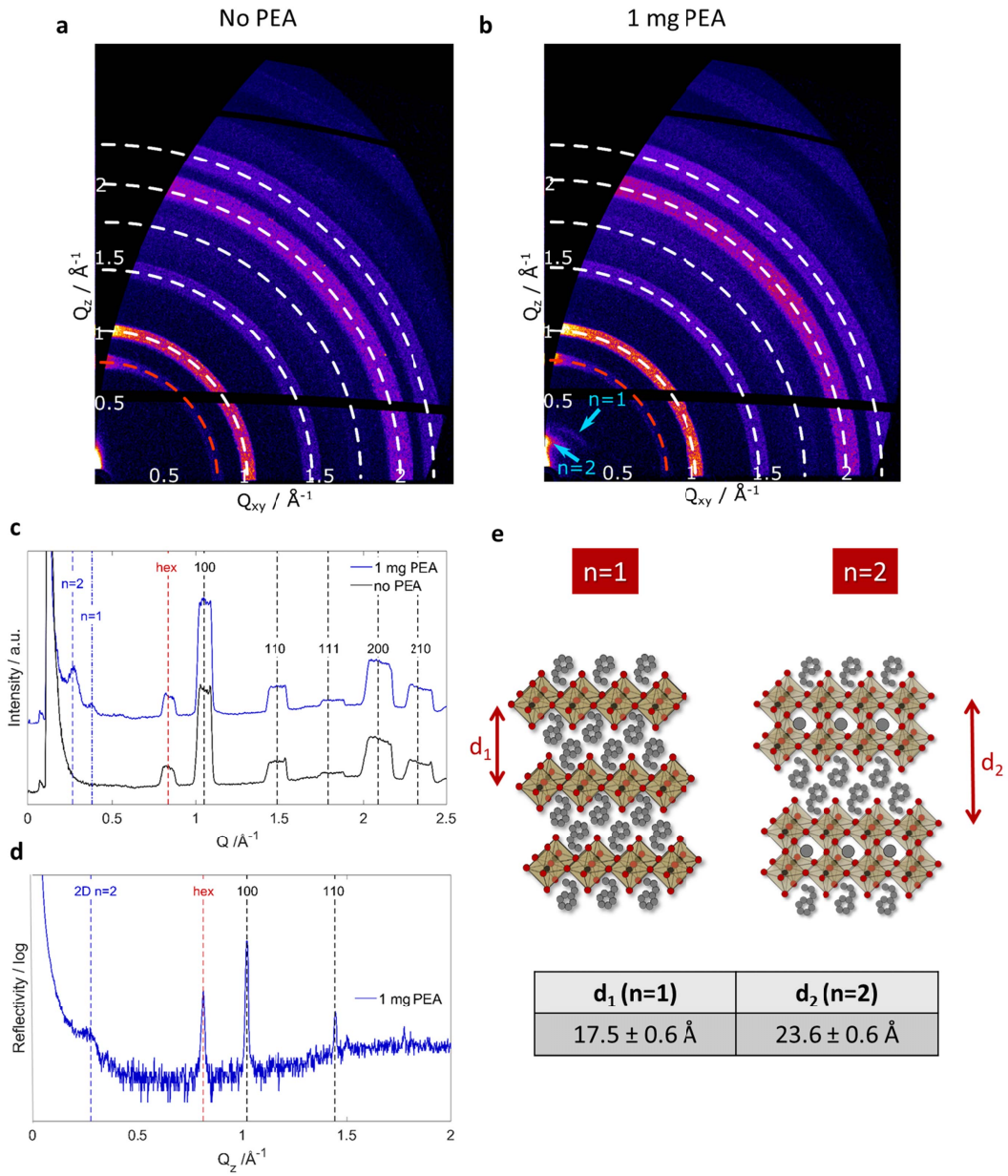

d_1 (n=1)	d_2 (n=2)
17.5 ± 0.6 Å	23.6 ± 0.6 Å

Figure S15: ***a,b,*** *Reciprocal space maps from gracing incidence wide angle X-ray scattering of perovskite films with and w/o PEAI surface treatment.* ***c,*** *radial profile obtained by azimuthal integration of reciprocal space maps evidencing the presence of (predominant n=2) 2D phase in the case of PEAI treated perovskite films.* ***d,*** *X-ray reflectivity measurement probing the z-axis not covered by GIWAXS measurements, also evidencing the n=2 2D Phase.* ***e,*** *schematic illustrations (top) and layer spacing calculated from the peak positions (bottom). The difference d_2-d_1 of ~ 6 Å corresponds with the height of one PbX_6 octahedron, indicating the presence of n=1 and n=2 layered structures.*

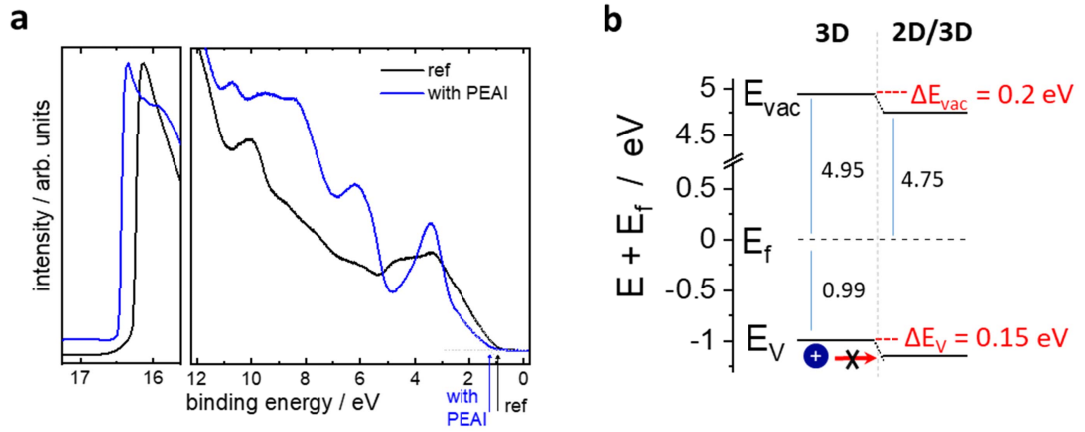

Figure S16: ***a,*** *UPS measurement of a reference 3D sample and a sample treated with PEAI. The shape of the density of states significantly changes due to the modification by PEAI.* ***b,*** *resulting energy level diagram of* E_{vac} *and* E_V *aligned at* E_f *of pristine 3D and PEAI treated 2D/3D perovskite.*

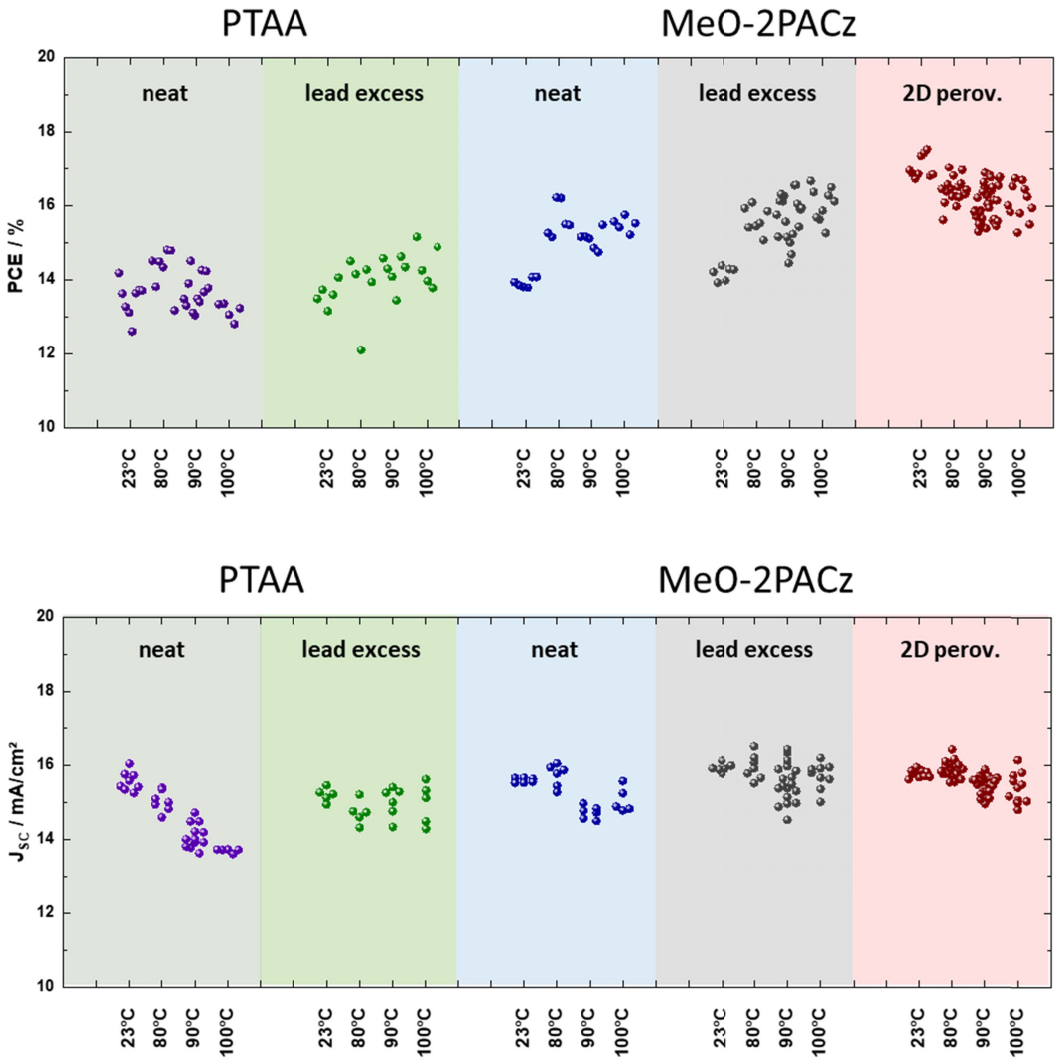

Figure S17: Comparison of the power conversion efficiency (top) and sort circuit current (bottom) with various annealing temperatures after the EEL deposition.

E_g / eV	V_{OC} / V	FF / %	PCE / %	J_{SC} / mA/cm²	E_g/e-V_{OC}	Reference
1.8	1.05	74	11.14	14.34	0.75	Nano Lett. 2016, 16, 12, 7739
1.8	1.12	58	9.8	15.1	0.68	Science. 2016, 354, 6314, 861
1.87	1.21	77	10.6	11.4	0.65	ACS Energy Lett. 2018, 3, 1, 214
1.82	1.3	65	11.6	12.9	0.52	Nano Lett. 2018, 18, 6, 3985
1.83	1.33	63	7.5	10.2	0.5	
1.84	1.35	57	3.3	5.1	0.49	
1.82	1.29	64	11.5	13.8	0.53	J. Phys. Chem. Lett. 2018, 9, 12, 3779
1.82	1.2	69	12.5	15.1	0.62	Adv. Mater. 2017, 29, 34, 172140
1.8	1.25	75	15.8	17.1	0.55	Sol. RRL 2020, 4, 7, 2000098
1.8	1.17	79	17	18	0.63	ACS Energ. Lett. 2020, 5, 8, 2728
1.84	1.19	78	16.2	17	0.65	
1.88	1.19	77	15.2	16.5	0.69	
1.86	1.28	73	15.2	15.3	0.58	Adv. Funct. Mater. 2018, 28, 35, 1803130
1.85	1.34	81	16.8	15.6	0.51	This work

Table S1: Cell characteristics of solar cells with E_g between 1.8 and 1.9 eV taken from literature (this table is the source for the data points in Figure 2e)

Supplementary Note 4. Determination of the Schottky-barrier at the interface of tin oxide and molybdenum oxide.

To assess the rectifying behavior inferred by the SnO_x/MoO_x interface, we prepared devices with a layer sequence ITO/SnO_x (20 nm)/MoO_x (5 nm)/gold. Forward bias refers to a positive bias of the MoO_x electrode with respect to the SnO_x electrode. Typically, rectifying current-voltage characteristics are found (Figure S18 a). We have used a standard diode model

$$I = I_O \left(\exp\left(\frac{q(V - IR_s)}{nk_BT}\right) - 1\right) + \frac{V - IR_s}{R_{sh}}$$

to fit the current-voltage characteristics. There, q is the elementary charge, n is the ideality factor, R_s and R_{sh} are the series and shunt resistance, respectively. I_O denotes the saturation, which can be expressed by $I_O = A \cdot A^* \cdot T^2 \exp\left(-\frac{q\,\phi_b}{k_BT}\right)$ with A^* being the Richardson constant, ϕ_b denoting the Schottky-barrier height and A stating the area of the device ($A = 3.14 \times 10^{-2} cm^2$). According to Crowell $A^* = \frac{4\pi q m^* k_B^2}{h^3}$.[22] With the effective mass of tin-oxide $m^* = 0.4\ m_0 \longrightarrow A^* = 48\ \frac{A}{cm^2 K}$.[23] I_0 is obtained from a fit of the current-voltage characteristics as shown in Figure S18 b and ϕ_b can be derived. The temperature of the diodes has been varied on a temperature-controlled stage in the range of 220-370 K (Figure S18 c). At room temperature we find $\phi_b = 0.62\ eV$, which is in excellent agreement with the results of photoelectron spectroscopy. ϕ_b increases from 0.48 eV at 220K to 0.72 eV at 370K (Figure S18 d). Note, some variation of ϕ_b with temperature has been frequently observed in earlier studies of Schottky-barriers in other material systems, and they have been attributed to inhomogeneities.[24, 25]

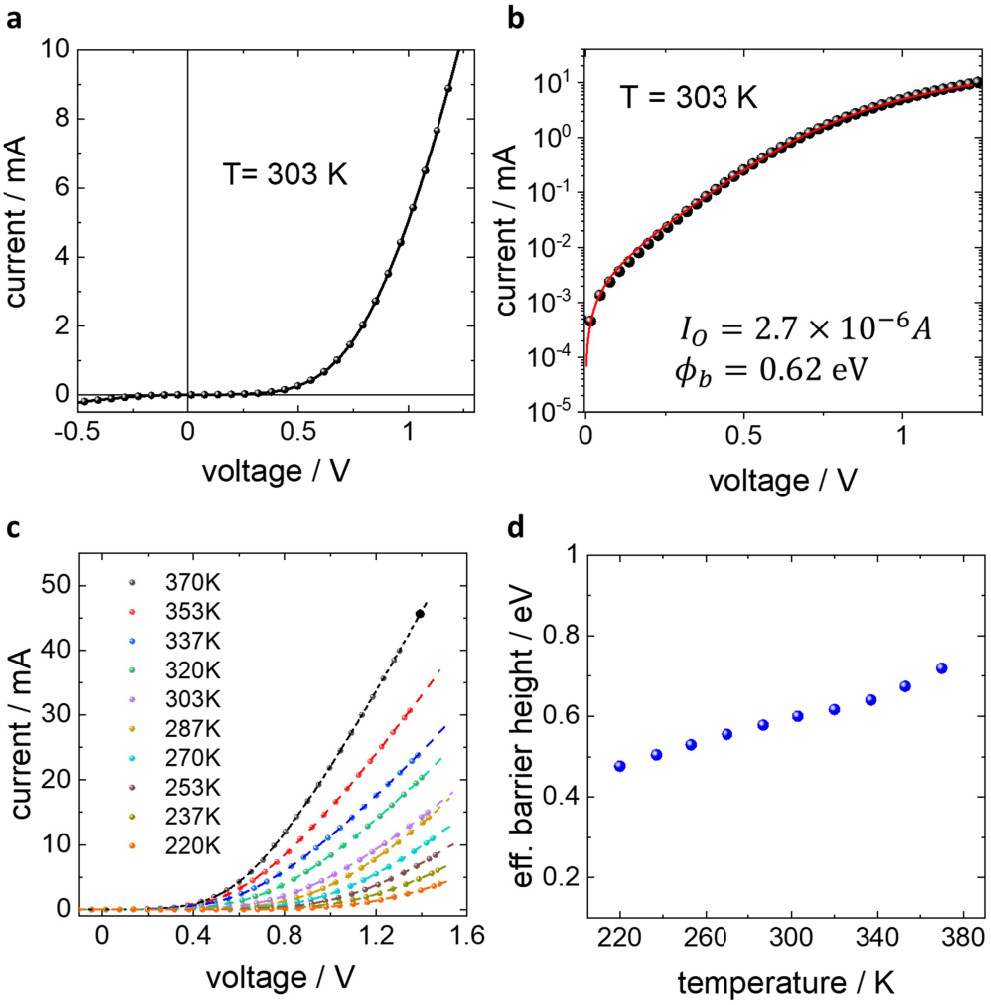

Figure S18: determination of Schottky-barrier height from the J-V characteristics. ***a,*** *forward J-V scans in linear and* ***b,*** *semi logarithmic scale.* ***c,*** *temperature dependent J-V scans and* ***d,*** *calculated barrier heights.*

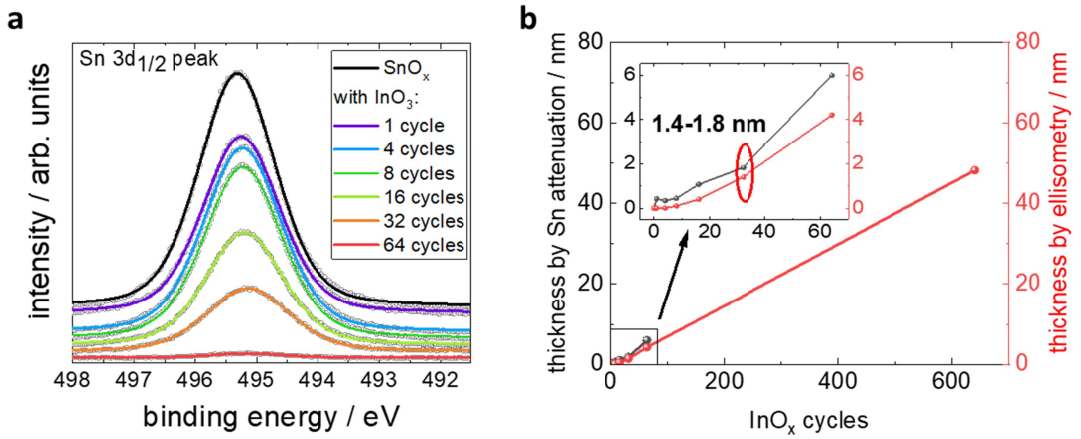

Figure S19: **a,** *Sn $3d_{1/2}$ XPS core level signal for pure SnO_x as well as for SnO_x covered by an increasing number of ALD cycles of InO_x.* **b,** *calculated layer thickness of the InO_x overlayer, extracted from the attenuation of the Sn core level peaks (left axis) or derived by ellipsometry (right axis). The inset shows the region of interest confirming a layer thickness of 1.4-1.8 nm for 32 growth cycles.*

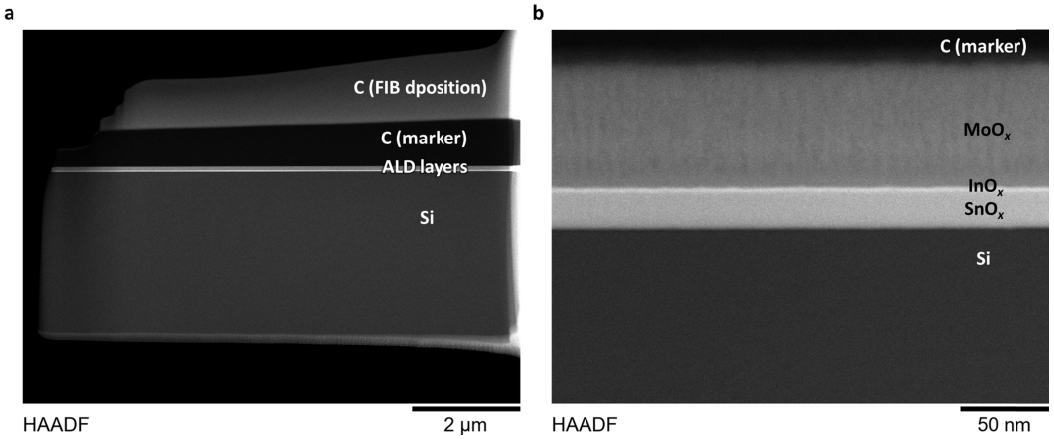

Figure S20: High angle annular dark field (HAADF)-STEM images of deposited SnO_x / InO_x / MoO_x layers on a silicon substrate at ***a,*** *2 µm and* ***b,*** *50 nm scales showing continuous ALD growth of both SnO_x and InO_x layers.*

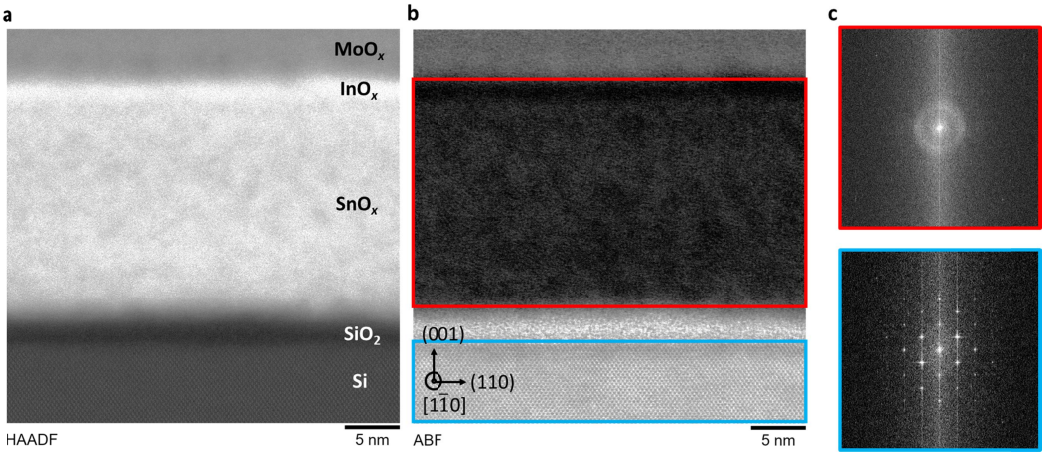

Figure S21: ***a,*** *High angle annular dark field (HAADF) and* ***b,*** *annular bright field of a silicon / native oxide / SnO_x / InO_x / MoO_x stack and* ***c,*** *respective fast Fourier transformed images of SnO_x / InO_x (top, red frame) and Si (bottom, blue frame) showing the contrast between the crystalline silicon wafer and the amorphous ALD layers covering it.*

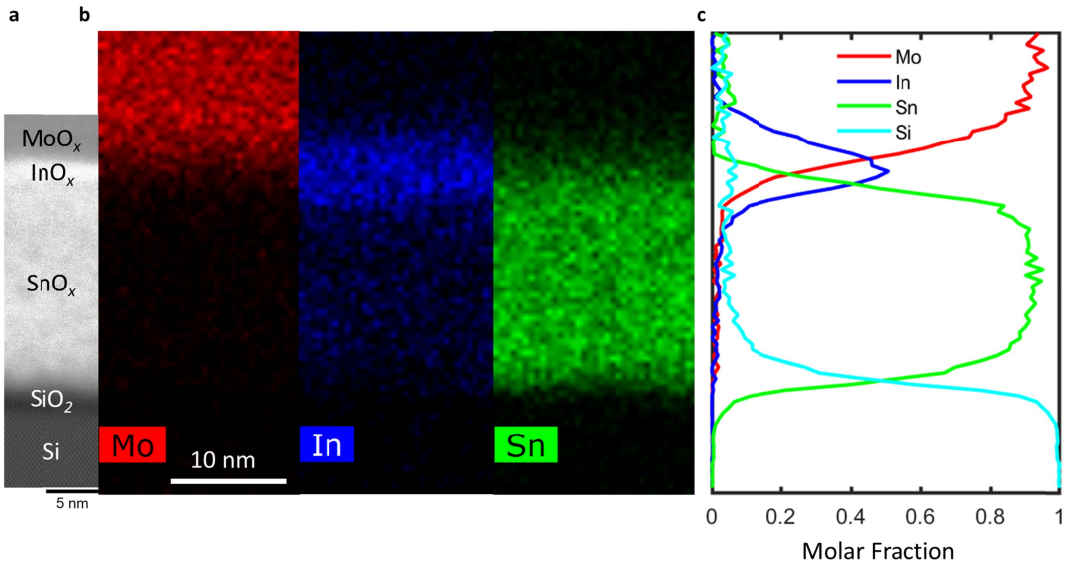

Figure S22 ***a,*** *High angle annular dark field (HAADF) measurement of silicon / SnO_x / InO_x / MoO_x and* ***b,*** *respective EDS elemental maps. The EDS count maps of In-L_α and Sn-L_α are plotted together with Mo-L_α. However, as In-L_α (3.29 eV) are very close to Sn-L_α (3.44) and overlap with Sn-L_n (3.27 eV), there are spurious counts inside the SnO_x layer that contribute to the In-L_α integration window. To separate the overlapping signals, we applied multivariate statistical analysis to separate EDS signals from the InO_x and SnO_x layers.[8,9] The resulting line profiles of Mo, In, and Sn are plotted in* ***c,*** *According to these line profiles, each layer is clearly separated. The soft edges of the elemental profiles (width about 2 nm) result from roughness of the layers (~2 nm, see Figure S23) and the collection of the EDS signals from the entire 100 nm thick TEM lamella. Therefore, we note that the EDS data does not indicate interdiffusion of elements between the layers.*

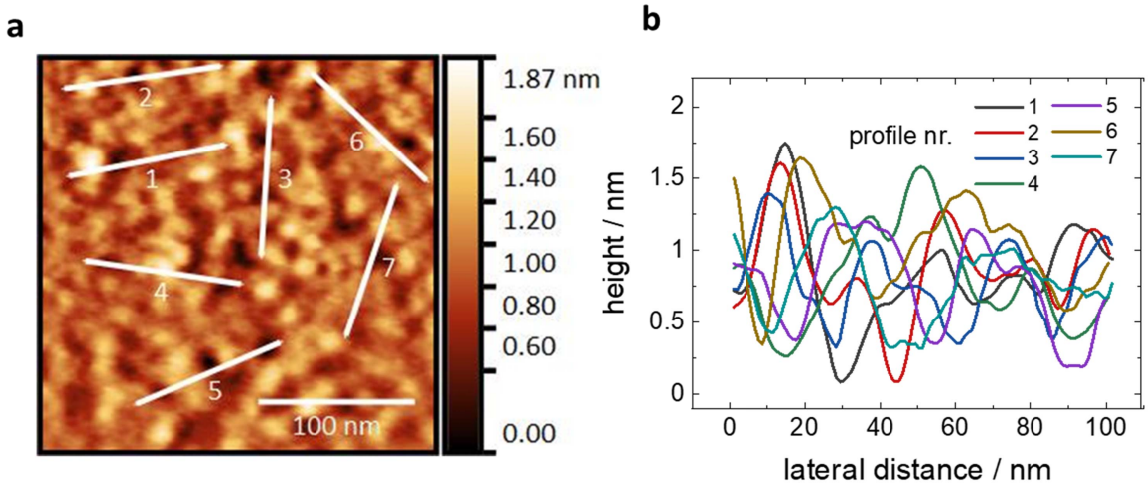

Figure S23: ***a,*** *Topography of a 20 nm thick tin oxide layer grown by ALD on a silicon substrate. Seven 100 nm traces are marked, indicating the extracted height profiles, shown in* ***b.***

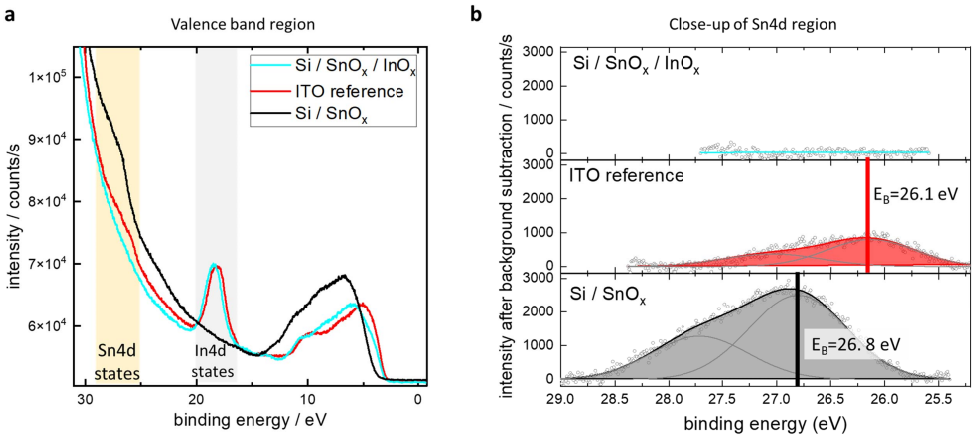

Figure S24: UV photoelectron spectroscopy measurements on SnO_x, SnO_x/InO_x, as well as an ITO reference layer using HeII excitation at 40.81 eV. ***a,*** *valence band region of the three samples, showing semi-core signals of Sn4d and In4d.* ***b,*** *Close-up of the Sn4d region, after a linear background subtraction has been performed. The data is fitted by two peaks corresponding to the $Sn4d_{5/2}$ and $Sn4d_{3/2}$ doublet. In contrast to the ITO and the SnO_x layers, for the InO_x (32 cycles; thickness of 1.5 nm) on top of SnO_x no signal of the Sn4d semi-core levels could be detected. With an estimated sampling depth of about 1 nm, this result indicates that, if there would be mixing of the InO_x and the SnO_x layer, it would be limited to the first 5 Angstroms of the InO_x layer adjacent to the SnO_x.*

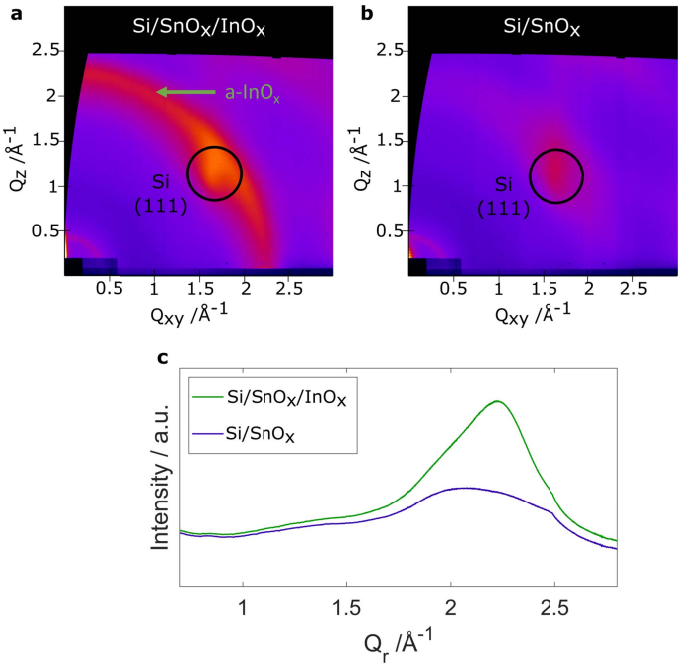

Figure S25: Bulk GIWAXS measurements of ***a,*** *20 nm InO_x on top of 20 nm SnO_x and* ***b,*** *only 20 nm SnO_x on top of a silicon substrate (incidence angle 0.3°, probing depth >500nm). With the probing depth exceeding the deposited layer thickness, some reflection due to the [111] planes of the Si substrate can also be seen (marked by a circle).* ***c,*** *Radial profiles of the data shown in a and b.*

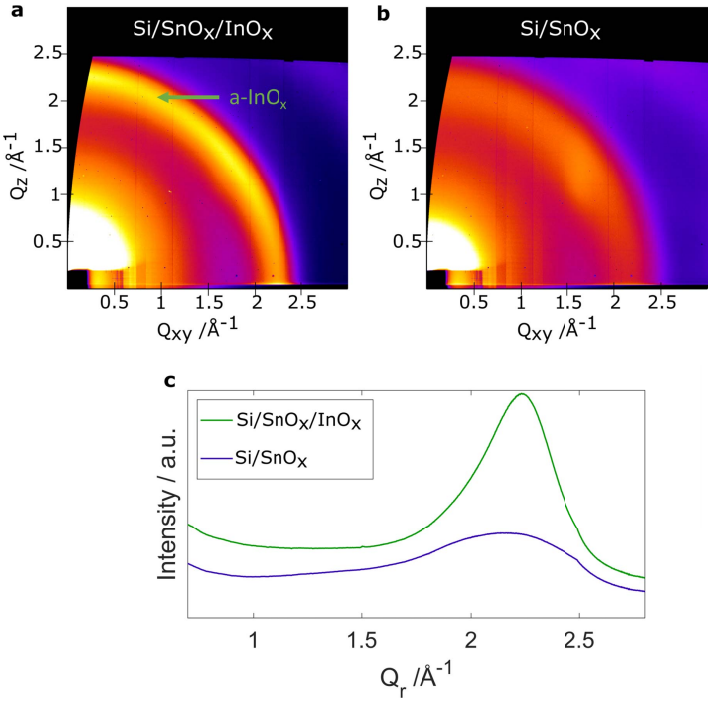

Figure S26: Surface GIWAXS measurements of ***a,*** *20 nm InO_x on top of 20 nm SnO_x and* ***b,*** *only 20 nm SnO_x on top of a silicon substrate (incidence angle 0.12° probing depth of about 2 nm) as well as* ***c,*** *respective radial profiles.*

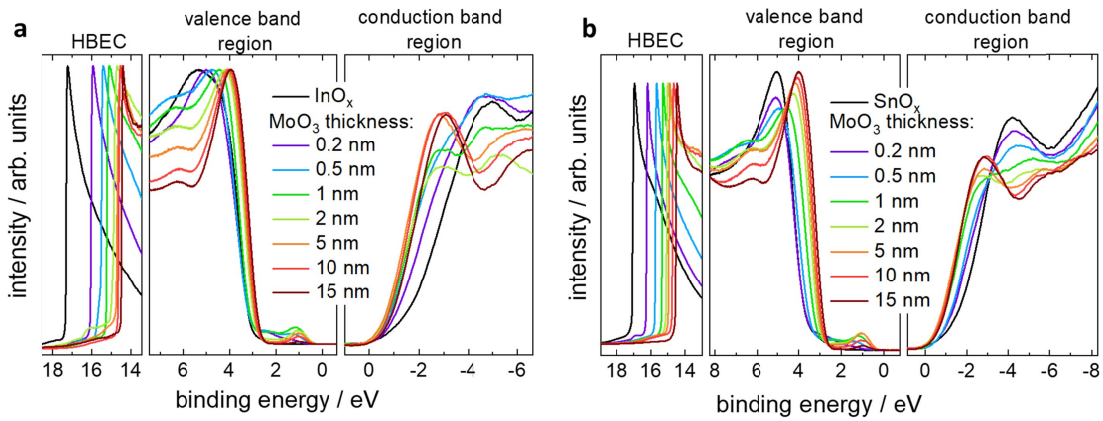

Figure S27: Combined UPS and IPES measurements of the interface between ***a,*** *InO_x (32 cycles) and MoO_3 as well as* ***b,*** *SnO_x and MoO_3. The high binding energy cutoff in the left panels shows the change in work function. For the IPES measurement only the smoothed data curves are shown. HBEC denotes the high binding energy cut-off region.*

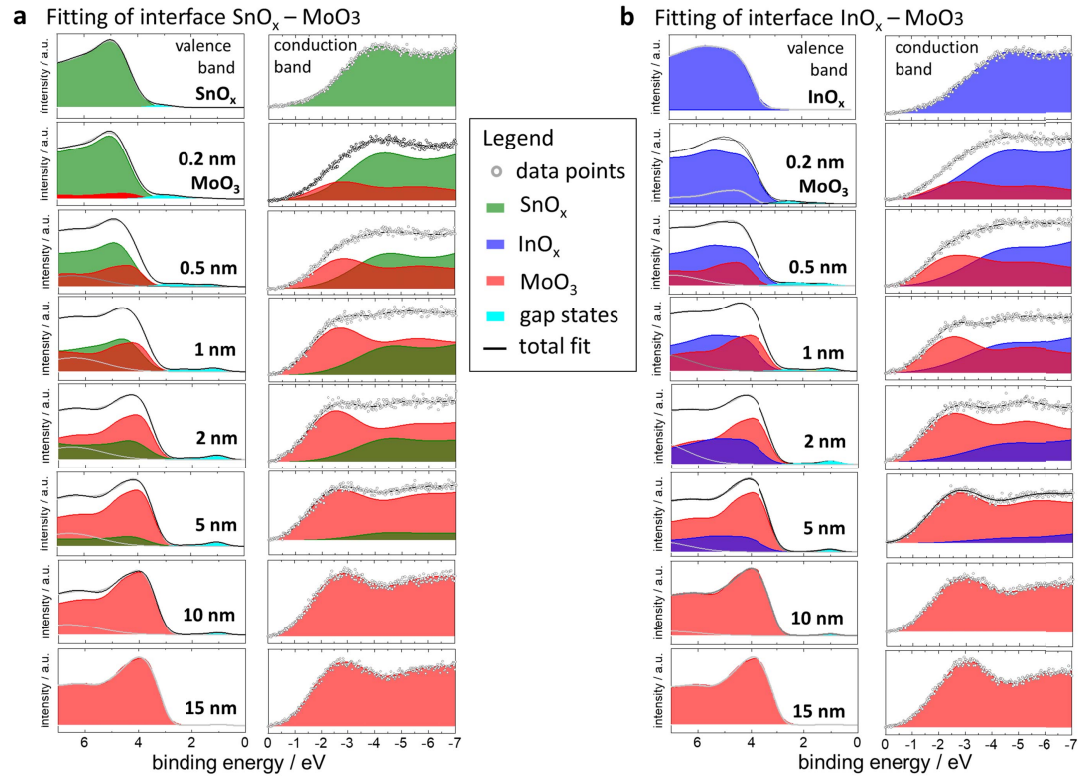

Figure S28: Detailed analysis of the UPS and IPES measurements (presented in Figure S27) of ***a,*** *interface between SnO_x and MoO_3 and* ***b,*** *InO_x (32 cycles) and MoO_3. The individual contributions to the density of states of the three metal oxides were fitted into the UPS spectra (left panels) and IPES spectra (right panels) in order to separate the contributions to the density of states of the substrates and the MoO_3 overlayer. From these fits the onsets of the VB and CB are extracted which are shown in Figure S29 and which are used to generate the energy level diagram (Figure 3d) in the main article.*

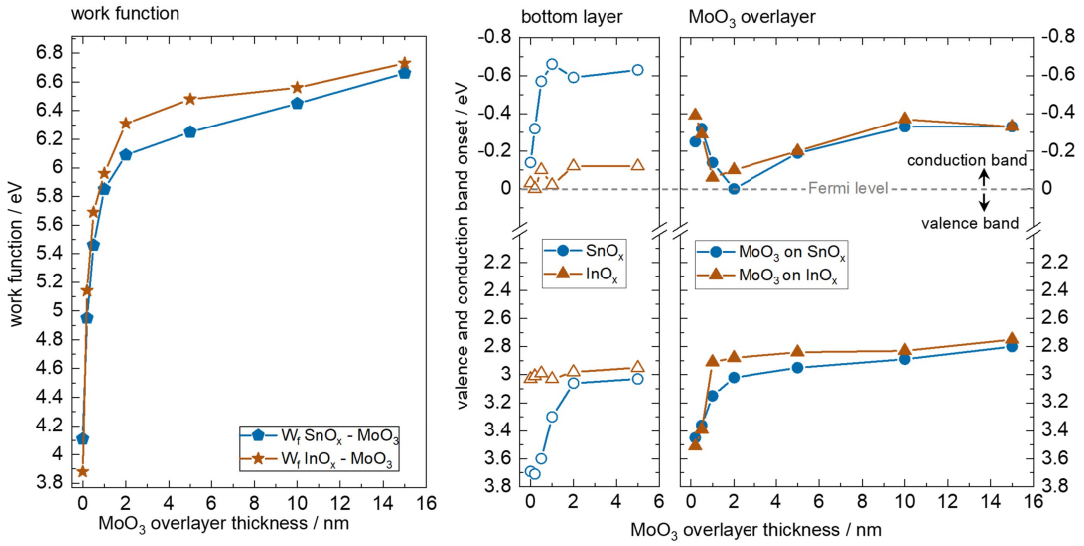

Figure S29: Plot summarizing the extracted energy values from Figures S27 and S28. The left panel shows the change in W_f with increasing MoO_3 thickness. The right panels show changes in VB and CB onset for the underlying substrate layers (SnO_x or InO_x) as well as the values for the MoO_3 overlayers on both substrates. While the upward bending of MoO_3 is similar in both cases, a distinct difference if found between the two substrates, where only SnO_x exhibits a detrimental upward bending of the VB and CB towards the interface.

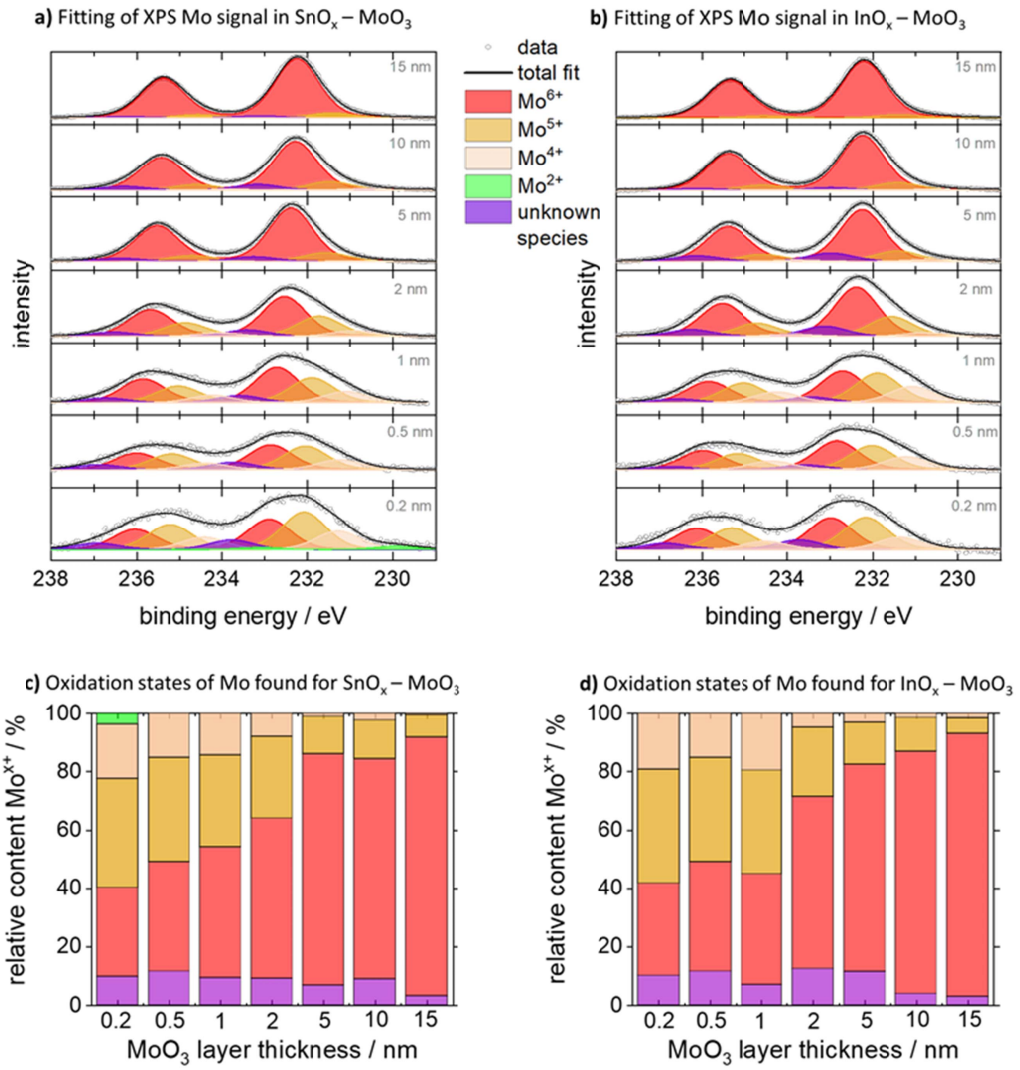

Figure S30: Mo core level signals of MoO_3 on **a,** *SnO_x and* **b,** *InO_x fitted by Voight profiles. For thick layers of MoO_3 the predominant oxidation state is Mo^{6+} as expected. For thinner MoO_3 layers, i.e. closer to the interface, additional oxidation states of Mo^{5+}, Mo^{4+}, and Mo^{2+} occur, possibly due to an increased number of oxygen vacancies. The relative content of each species is given in subfigures* **c,** *and* **d,** *for SnO_x and InO_x, respectively. Surprisingly, an additional Mo feature (violet) has to be included in the fit. The presence of an Mo bond at a binding energy larger than the one of Mo^{6+} in MoO_3 indicates the presence of a species with stronger electron withdrawing properties (relative to Mo). Its origin is currently unclear. Since oxygen is the only element with a higher electronegativity than Mo in these samples (therefore capable of increasing the apparent core level binding energy), we can speculate on a molybdate species such as In_2MoO_4. However, further tests are needed to identify possible reaction species; this is ongoing work and will be discussed in a separate publication.*

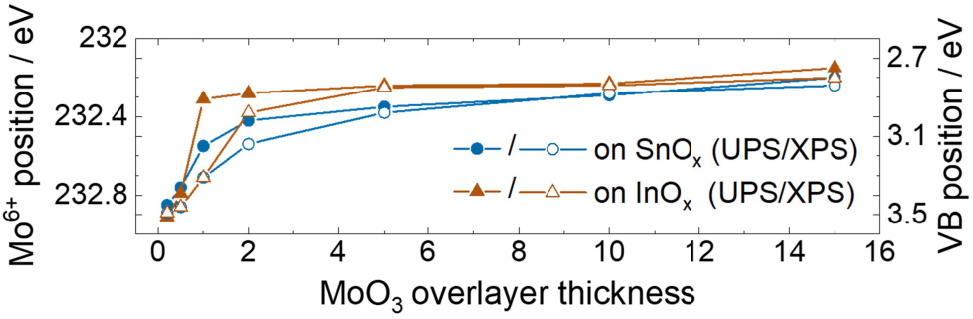

Figure S31: Change in energy levels of the MoO_3 layer as function of film thickness on either SnO_x (blue) or InO_x (brown). The filled symbols represent the change in VB onset, already presented in Figure S27. The open symbols represent the change in the Mo^{6+} core level signal, extracted from the fits in Figure S28. Slight differences at low coverage are likely due to differences in probing depth (~2 nm for UPS and ~10 nm for XPS), but overall the two measurements agree well and show the band bending present at this interface of the interconnecting layer.

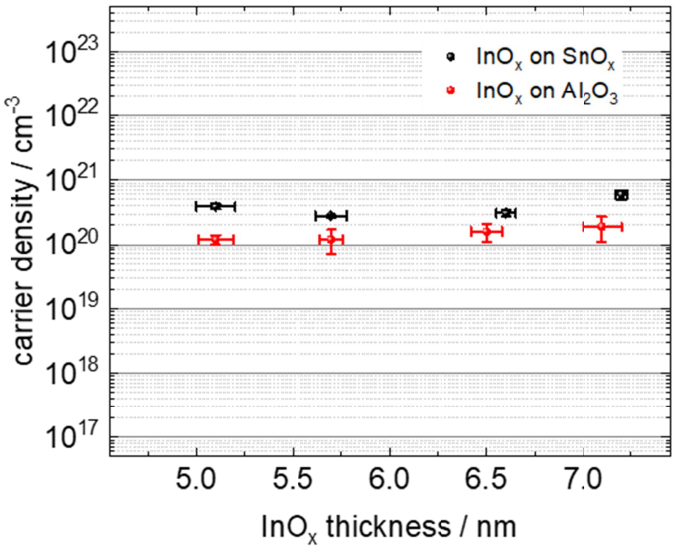

Figure S32: Charge carrier densities (and respective standard error) of InO_x layers of various thickness grown either on a SnO_x or an Al_2O_3 seed layer.

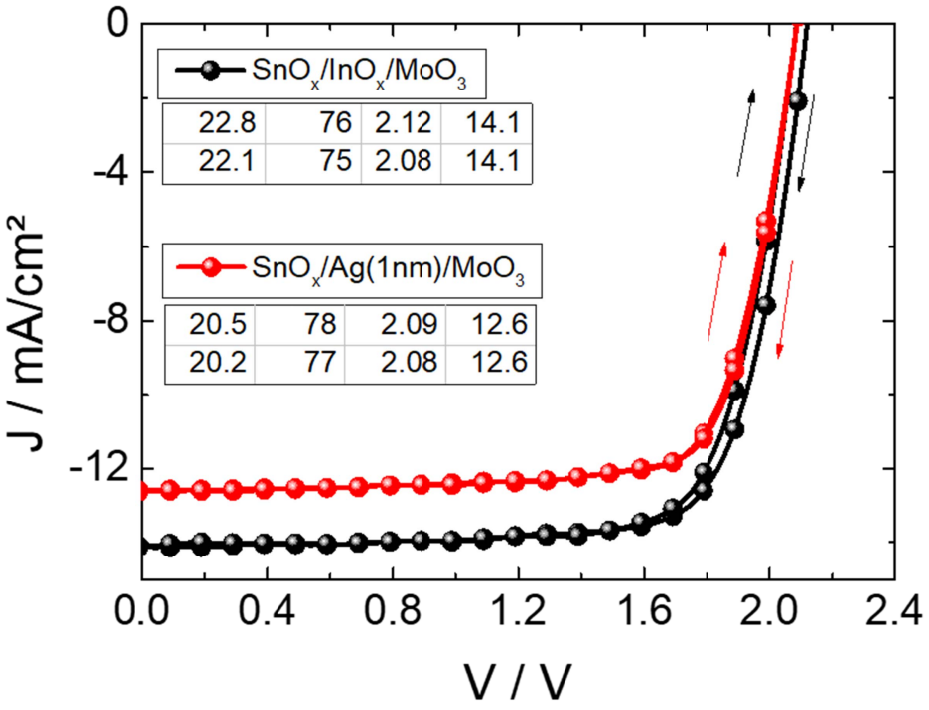

Figure S33: Comparison of representative J/V characteristics of perovskite/organic tandem cells employing either 1 nm of evaporated silver or ~1.5 nm InO_x deposited by atomic layer deposition as interconnecting layer. No MgF_2 AR coating was applied on the backside of the glass substrate, here.

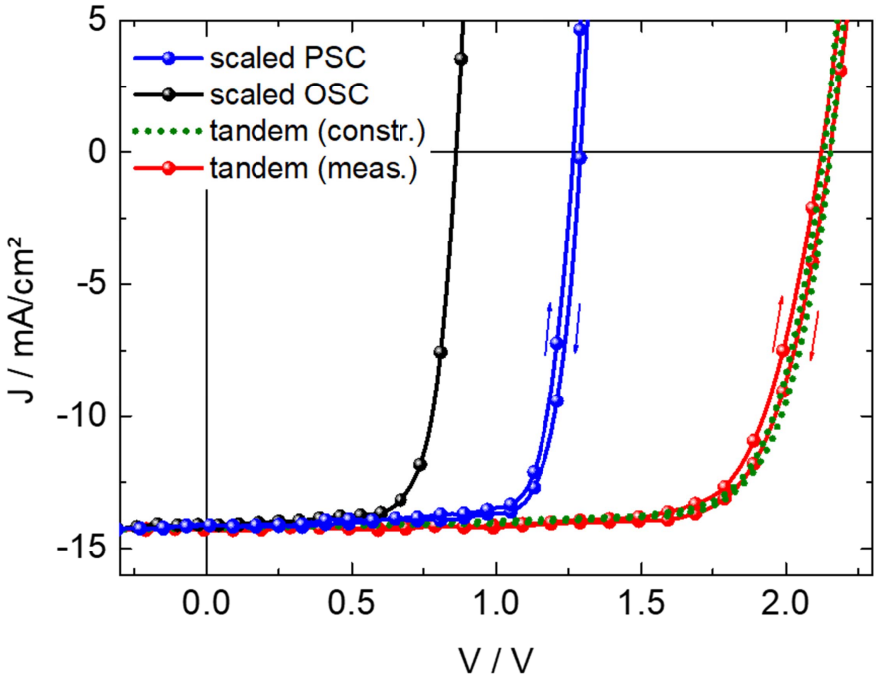

Figure S34: Construction of the theoretical J/V curves of the tandem device from the serial connection of both sub-cells. To emulate the J/V characteristics of the sub-cells, the measured J/V characteristics of representative single junction devices have been scaled to generate the respective short circuit current density that was derived from EQE results of the sub-cells in the tandem device.

		PCE* / %	FF / %	V_{OC} / V	J_{SC} / mA/cm²
PSC in tandem	reverse	14.5	80	1.29	14.1
	forward	14.1	79	1.27	14.1
OSC in tandem	invariant	8.9	73	0.86	14.1
constructed tandem	reverse	23.5	77	2.15	14.2
	forward	23.2	77	2.13	14.2
measured tandem	reverse	23.7	78	2.15	14.2
	forward	23.0	76	2.12	14.2

** calculated for P_{in} = 100 mW/cm²*

Table S2: Solar cell characteristics of the devices shown in Figure S34.

		PCE / %	FF / %	V_{OC} / V	J_{SC}/mA/cm²
perovskite subcell	reverse	16.0±0.5 [16.8] *(16.8)*	80±1 [81] *(82)*	1.30±0.02 [1.34] *(1.34)*	15.5±0.2 [15.6] *(15.9)*
	forward	15.7±0.7 [16.4] *(16.7)*	78±2 [80] *(82)*	1.29±0.02 [1.33] *(1.33)*	15.5±0.3 [15.5] *(16.0)*
organic subcell	invariant	16.5±0.4 [17.5] *(17.5)*	74±1 [75] *(77)*	0.86±0.01 [0.87] *(0.87)*	26.0±0.5 [26.7] *(26.9)*
tandem	reverse	23.4±0.5 [24.0] *(24.2)*	80±1 [80] *(83)*	2.12±0.02 [2.15] *(2.17)*	13.9±0.2 [14.0] *(14.5)*
	forward	22.7±0.7 [23.9] *(23.9)*	78±2 [79] *(83)*	2.13±0.03 [2.14] *(2.17)*	13.8±0.4 [14.1] *(14.4)*

Table S3: Overview of statistic cell characteristics of the single junctions and tandem cells derived from J/V scans. The numbers in square brackets represent the respective champion cells, the round brackets are the highest singular values that were achieved (not necessarily in the same solar cell). This data was calculated from a total of 34 perovskite, 60 organic and 48 tandem solar cells, fabricated in various batches by different persons.

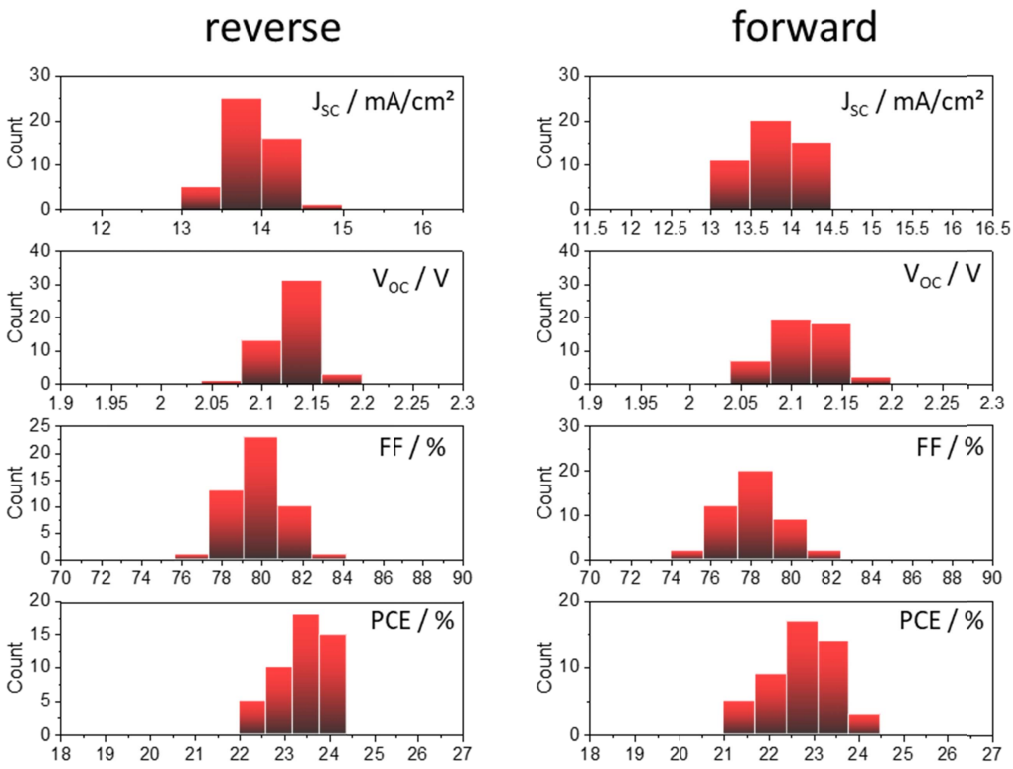

Figure S35: Statistics (binned) of 48 perovskite/organic tandem solar cells with InO_x interconnect

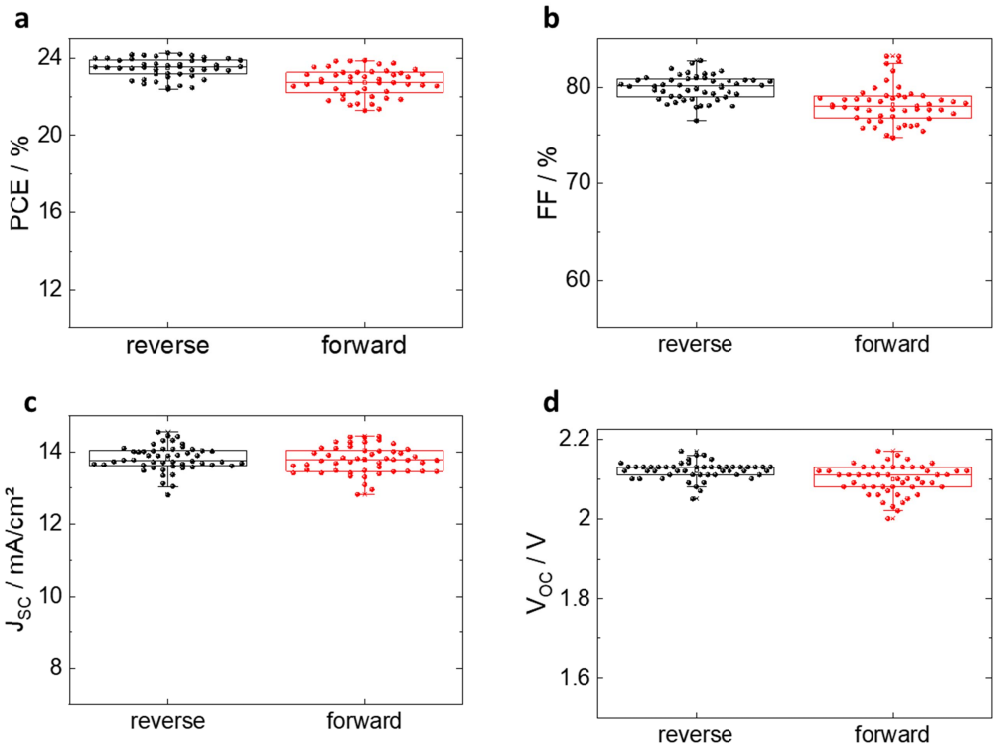

Figure S36: Statistics (box plot, 25% - 75% with mean line and data overlay) of 48 perovskite/organic tandem solar cells with InO_x interconnect.

Supplementary Note 5. Stress due to the certification process of the tandem solar cell

The certification procedure involves the measurement of the external quantum efficiency prior to J-V certification. This EQE measurement procedure, which is done in ambient air, takes about 1 hour and inflicts some severe asymmetric stressing of each sub-cell due to the necessary monochromatic light biasing.[6] These EQE measurement conditions infer some degradation of the cell, that would not occur under "normal" operation of the cell under AM 1.5 solar illumination. This is clearly visible if one compares the integrated current values derived from the certified EQE measurement (≥ 14 mA/cm² for both sub-cells, Figure S37, S38) with the value of 13.2 mA/cm² resulting from a J-V measurement thereafter (Figure S40). Nevertheless, the Fraunhofer ISE CalLab certified an efficiency of 23.1 per cent for this stressed cell (Figure S39) and confirmed 23.7 per cent for a sister cell, that had not undergone the stressing in a prior EQE measurement. In this case the spectral illumination characteristics calibrated for the certified sister cell were used. The latter efficiency is identical to what we have measured for the same cell prior to shipping the cell to the Fraunhofer ISE CalLab (Figure S40). As such, we can confirm the validity of our measurement. The respective value is labeled as "confirmed" in the main part of the paper.

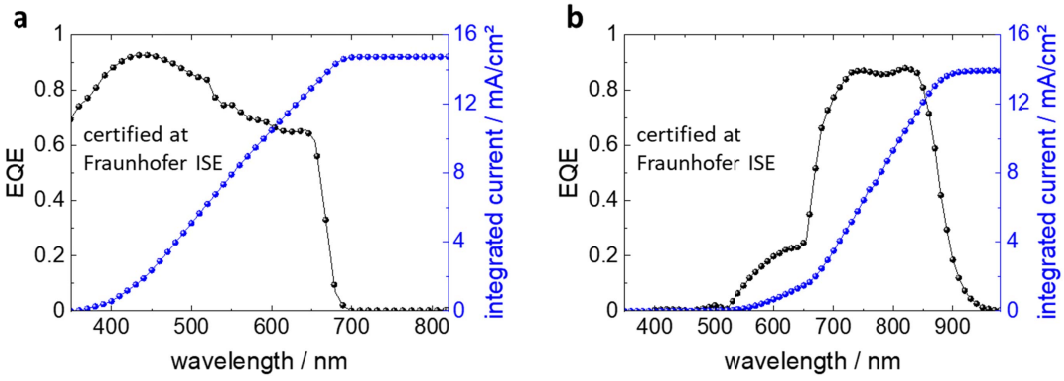

Figure S37: Certified EQE spectra measured at the ISE Fraunhofer CalLab (also see Figure S38) as well as derived integrated current values of ***a****, the perovskite and* ***b****, the organic sub-cell.*

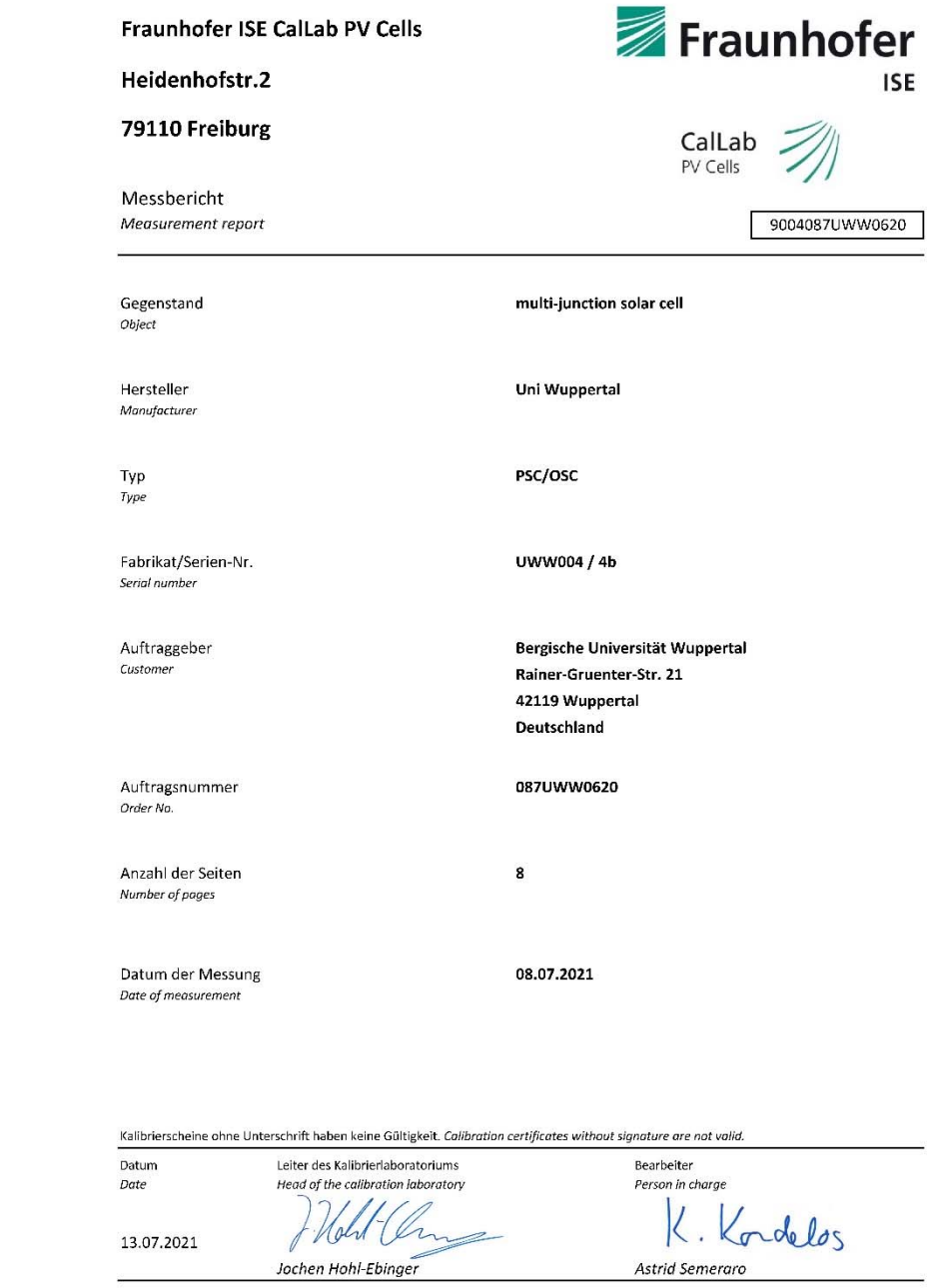

Fraunhofer ISE CalLab PV Cells

Heidenhofstr.2

79110 Freiburg

Fraunhofer ISE

CalLab PV Cells

Messbericht
Measurement report

9004087UWW0620

Gegenstand *Object*	**multi-junction solar cell**
Hersteller *Manufacturer*	**Uni Wuppertal**
Typ *Type*	**PSC/OSC**
Fabrikat/Serien-Nr. *Serial number*	**UWW004 / 4b**
Auftraggeber *Customer*	**Bergische Universität Wuppertal** **Rainer-Gruenter-Str. 21** **42119 Wuppertal** **Deutschland**
Auftragsnummer *Order No.*	**087UWW0620**
Anzahl der Seiten *Number of pages*	**8**
Datum der Messung *Date of measurement*	**08.07.2021**

Kalibrierscheine ohne Unterschrift haben keine Gültigkeit. *Calibration certificates without signature are not valid.*

Datum *Date*	Leiter des Kalibrierlaboratoriums *Head of the calibration laboratory*	Bearbeiter *Person in charge*
13.07.2021	*Jochen Hohl-Ebinger*	*Astrid Semeraro*

Figure S38/1 certificate for EQE values

Fraunhofer ISE

9004087UWW0620

CalLab PV Cells

1. Beschreibung des Messgegenstandes

Description of the measurement object

Das Messobjekt ist eine Solarzelle, Typ: PSC/OSC. Die Stabilität der Solarzelle wurde nicht untersucht.
The device under test is a PSC/OSC solar cell. The temporal stability of the solar cell performance was not controlled.

2. Messverfahren

Measurement procedure

Bestimmt wird der Wert der absoluten differentiellen spektralen Bestrahlungsstärkeempfindlichkeit im Wellenlängenbereich ca. 300-1200 nm bei dem angegebenen Kurzschlussstrom. Die Kalibrierung der Solarzelle wurde mit einem Lasermonochromator mit dem DSR-Messverfahren /1/ und entsprechend /2/ durchgeführt. Die Messung wird im Zweistrahlverfahren durchgeführt und verwendet gleichzeitig:
a) eine stationäre Biasbestrahlung mit Bestrahlungsstärken E_B, welche jedoch nicht explizit gemessen werden. Ihre Variation erlaubt unterschiedliche Kurzschlussströme I_{SC} (E_B), sowie
b) eine zeitlich modulierte, quasi-monochromatische Messstrahlung. Ihre Bestrahlungsstärke wird bestimmt mit einer primarkalibrierten Referenzsolarzelle (rückgeführt: PTB).
The absolute differential spectral responsivity is determined in a wavelength range from 300 nm to 1200 nm at a short circuit current bias.eee The measurement is done with laser-monoochromator setup with the DSR method according to /1/ and /2/ in a two-beam geometry, using the two irradiation beams simultaneously:
a) A stationary bias irradiation with irradiances E_B (not measured explicitly).
The variation of E_B allows different short circuit currents I_{SC} (E_B),
b) A time-modulated quasi-monochromatic measurement irradiation. The irradiance is determined by a primary calibrated reference solar cell (PTB).

Rückführung der Referenzsolarzelle/*Traceability of the reference solar cell*:

Identitäts-Nr. / *Identity-Nr.*:	Kalibrierschein-Nr./ *Certificate-Nr.*:	Rückführung/ *Traceability*:
020059	47033-PTB-21	PTB

Figure S38/2 certificate for EQE values

Fraunhofer ISE

CalLab PV Cells

9004087UWW0620

3. Messbedingungen

Measurement conditions

Der Arbeitspunkt der Solarzelle wird durch den Bias-Strom im I_{SC} definiert.

The operating point of the solar cell is defined by a bias current under short circuit conditions.

	top cell	bot cell
Bias Strom/*Bias current*:	0 mA	0 mA
Bias Spannung/Bias voltage:	611.54 mV	702.36 mV
Nominalwert der Temperatur des Messobjekts/ *Nominal Value of the temperature of the object:*	25 °C	25 °C

Die Klemmenspannung der Solarzelle wird durch einen Strom-Spannungswandler auf unter 0,03 V_{OC} geregelt. Die Frequenz des getakteten quasimonochromatischen Messlichtes lag bei 133 Hz. Die spektrale Bandbreite (Halbwertsbreite) liegt unter 5 nm. Die Temperatur der Solarzelle wird mit einem Tastsensor ermittelt und auf (25±0,5)°C eingestellt.

The voltage at the solar cell is set to below 0.03 V_{OC} by a current-voltage-converter. The frequency of the chopped quasi-monochromtatic measurement light is at 133 Hz. The spectral bandwith (full width at half maximum) is below 5 nm. The temperature of the solar cell is determined by a sensor and adjusted to (25±0.5)°C.

Figure S38/3 certificate for EQE values

Fraunhofer ISE

CalLab PV Cells

9004087UWW0620

4. Messergebnis

Measurement results

top cell

Wellenlänge *Wavelength* / nm	$*\eta_{ext}$ /	*s* / $mA*W^{-1}*m^2$
310.0	0.0392	0.00002
320.0	0.478	0.00022
350.0	0.699	0.000344
360.0	0.743	0.0003759
370.0	0.771	0.0004009
380.0	0.805	0.0004299
390.0	0.849	0.00046565
400.0	0.877	0.0004934
410.0	0.899	0.00051804
420.0	0.917	0.0005414
430.0	0.926	0.0005598
440.0	0.927	0.0005731
450.0	0.927	0.0005865
460.0	0.917	0.0005933
470.0	0.904	0.0005973
480.0	0.893	0.0006024
490.0	0.875	0.0006025
500.0	0.857	0.0006026
510.0	0.845	0.0006062
520.0	0.837	0.0006120
529.4	0.775	0.000577
540.7	0.746	0.000567
551.2	0.747	0.0005788
561.0	0.722	0.0005695
572.2	0.699	0.0005627
580.4	0.694	0.0005661
592.1	0.687	0.0005721
602.4	0.667	0.0005653
612.2	0.654	0.0005630
621.5	0.649	0.0005674
633.4	0.651	0.0005794
642.8	0.656	0.0005931
654.6	0.616	0.0005669
668.0	0.325	0.0003052
679.5	0.0693	0.0000662
690.0	0.0166	0.0000161
696.3	0.00626	0.0000061
700.0	0.000403	0.0000004
710.0	0.00252	0.0000025
740.0	0.00175	0.0000018
780.0	0.00218	0.0000024
820.0	0.00340	0.00000392
860.0	0.00280	0.0000034

Figure S38/4 certificate for EQE values

Fraunhofer ISE

CalLab PV Cells

9004087UWW0620

bottom cell

Wellenlänge *Wavelength* / nm	$^{*}\eta_{ext}$ /	s / mA*W^{-1}*m²
400.0	0.00477	0.0000027
420.0	0.00653	0.00000385
440.0	0.00521	0.00000321
460.0	0.000559	0.00000036
480.0	0.00910	0.0000061
500.0	0.0204	0.0000143
520.0	0.00794	0.0000058
561.0	0.123	0.0000969
580.4	0.163	0.0001324
602.4	0.202	0.0001707
612.2	0.211	0.0001816
621.5	0.224	0.0001951
633.4	0.229	0.0002034
643.9	0.231	0.0002091
654.6	0.259	0.0002380
667.8	0.485	0.0004541
679.5	0.659	0.0006289
690.0	0.729	0.0007055
694.6	0.741	0.0007228
700.0	0.774	0.0007607
710.0	0.811	0.0008085
720.0	0.840	0.0008493
730.0	0.865	0.0008857
740.0	0.869	0.0009030
750.0	0.871	0.0009170
760.0	0.867	0.0009246
770.0	0.861	0.0009304
780.0	0.857	0.0009386
790.0	0.859	0.0009520
800.0	0.864	0.0009702
810.0	0.873	0.0009926
820.0	0.880	0.0010124
830.0	0.875	0.0010189
840.0	0.863	0.0010171
850.0	0.810	0.0009665
860.0	0.716	0.0008641
870.0	0.589	0.0007195
880.0	0.444	0.0005482
890.0	0.306	0.0003825
900.0	0.200	0.0002523
910.0	0.123	0.0001574
920.0	0.0735	0.0000949
930.0	0.0442	0.0000577
940.0	0.0281	0.0000371
950.0	0.0112	0.0000150
960.0	0.00750	0.0000101
970.0	0.00303	0.0000041
980.0	0.00320	0.0000044

Figure S38/5 certificate for EQE values

Fraunhofer ISE

CalLab PV Cells

9004087UWW0620

bottom cell

Wellenlänge *Wavelength* / nm	$*\eta_{ext}$ /	s / mA*W^{-1}*m^2
980.0	0.00320	0.0000044

*Spektrale Bestrahlungsstärkeempfindlichkeit und externe Quanteneffizienz stehen in folgendem Zusammenhang / *Spectral responsivity and External Quantum Efficiency are related as follows:*

$$\eta_{ext}(\lambda) = \frac{J(\lambda)/q}{E(\lambda)/h\nu} = \frac{h\nu}{q}\frac{J(\lambda)}{E(\lambda)} = \frac{hc}{nq\lambda}\frac{s(\lambda)}{a} = 1239{,}8\frac{nm\cdot W}{A}\frac{s(\lambda)}{n\lambda a}$$

c: Vakuumlichtgeschwindigkeit/ *speed of light in a vacuum*
h: Planck'sches Wirkungsquantum/ *Planck constant*
q: Elementarladung/ *elementary charge*
n: Brechungsindex Luft/ *refraction index*
$\eta_{ext}(\lambda)$: externe Quanteneffizienz/ *external quantum efficiency*
$s(\lambda)$: spektrale Bestrahlungsstärkeempfindlichkeit/ *spectral responsivity*
a: Fläche/ *area*

Figure S38/6 certificate for EQE values

Fraunhofer ISE

9004087UWW0620

CalLab PV Cells

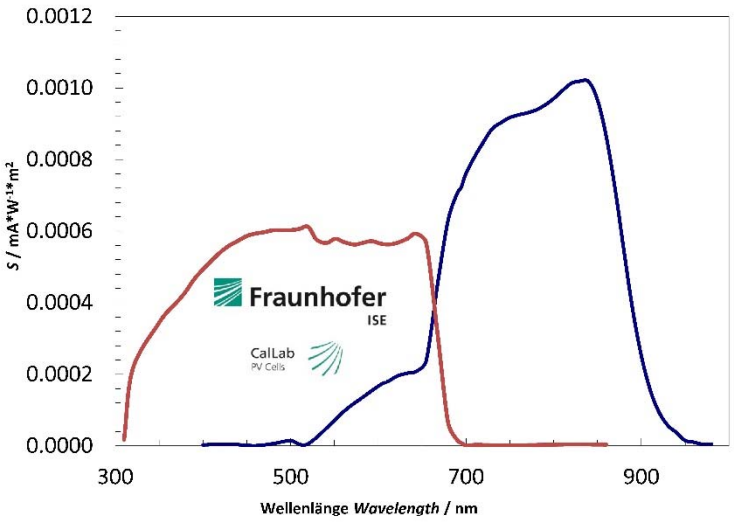

6. Literatur

Literature

/1/ J. Metzdorf, Calibration of Solar Cells. 1: *The Differential Spectral Responsivity Method*, Applied Optics 26 (1987) p.1701-1708

/2/ IEC 60904-8-Ed.3:2014, *Photovoltaic devices - Part 8: Measurement of the spectral responsivity of a photovoltaic (PV) device*

Figure S38/7 certificate for EQE values

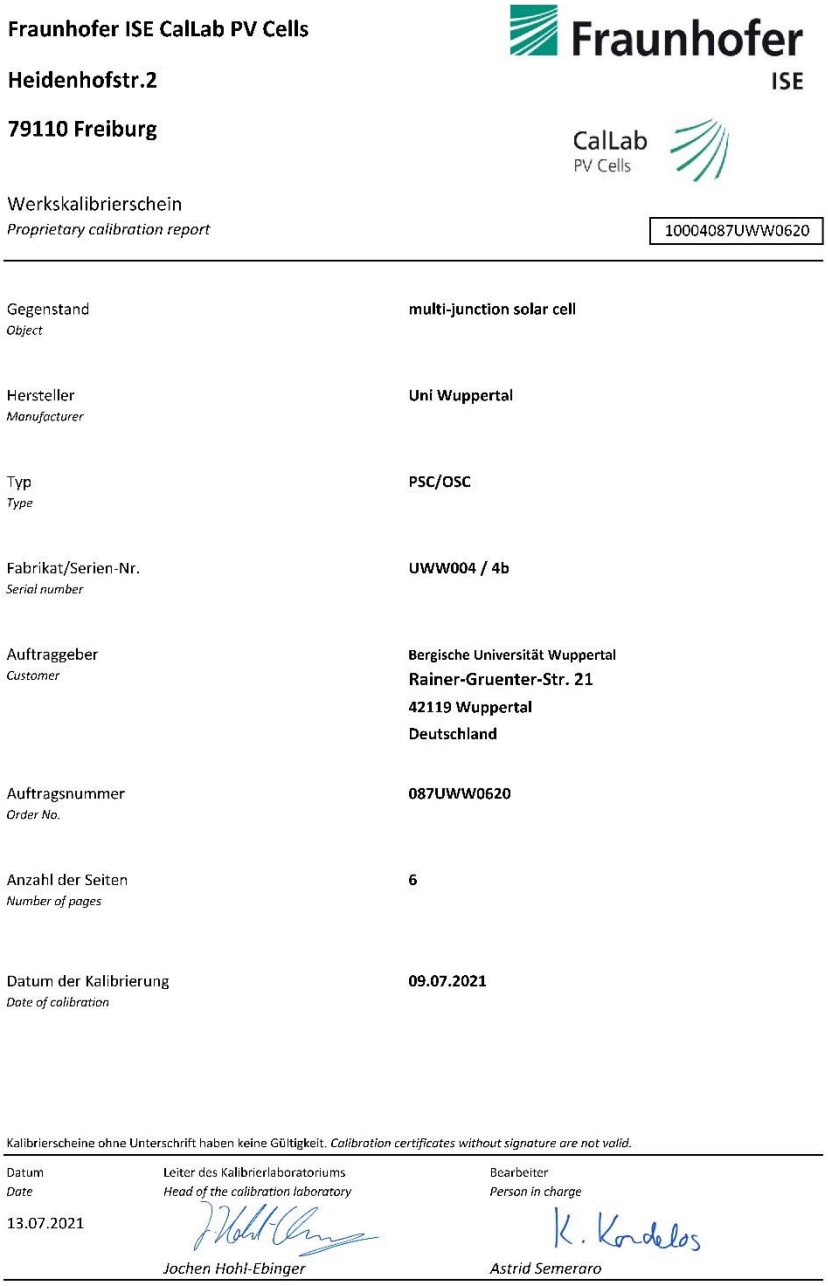

Fraunhofer ISE CalLab PV Cells

Heidenhofstr.2

79110 Freiburg

Fraunhofer ISE

CalLab PV Cells

Werkskalibrierschein
Proprietary calibration report

10004087UWW0620

Gegenstand *Object*	**multi-junction solar cell**
Hersteller *Manufacturer*	**Uni Wuppertal**
Typ *Type*	**PSC/OSC**
Fabrikat/Serien-Nr. *Serial number*	**UWW004 / 4b**
Auftraggeber *Customer*	**Bergische Universität Wuppertal** **Rainer-Gruenter-Str. 21** **42119 Wuppertal** **Deutschland**
Auftragsnummer *Order No.*	**087UWW0620**
Anzahl der Seiten *Number of pages*	**6**
Datum der Kalibrierung *Date of calibration*	**09.07.2021**

Kalibrierscheine ohne Unterschrift haben keine Gültigkeit. *Calibration certificates without signature are not valid.*

Datum *Date*	Leiter des Kalibrierlaboratoriums *Head of the calibration laboratory*	Bearbeiter *Person in charge*
13.07.2021	*Jochen Hohl-Ebinger*	*Astrid Semeraro*

Figure S39/1 certificate for J/V scan and stabilized power output

Fraunhofer ISE

CalLab PV Cells

10004087UWW0620

1. Beschreibung des Kalibriergegenstandes

Description of the calibrated object

Das Messobjekt ist eine multi-junction solar cell. Typ: OSC/PSC

The device under test is a OSC/PSC multi-junction solar cell .

2. Messverfahren

Measurement procedure

Die Kalibrierung des Kalibrierobjektes wird gemäß /1/ mit einem Zweilampen-DC-Sonnensimulator durchgeführt. Die Einstrahlung wird mit Hilfe einer Monitorzelle während der gesamten Messdauer aufgenommen und deren Schwankungen bezüglich der Messung korrigiert. Die Divergenz der Randstrahlen ist < 5°. Die Solarzelle wird auf einem Vakuumprobentisch thermisch stabilisiert.

The calibration of the test sample was performed at Standard Testing Conditions (STC) with a dual light steady-state solar simulator according to /1/. The irradiance is controlled with a monitor cell during the measurement in order to correct fluctuations. The divergence of the peripheral beams is < 5°. The solar cell is kept at a constant temperature

Rückführung der Referenzsolarzellen/*Traceability of the reference solar cells* :

Identitäts-Nr. / *Identity-Nr.* :	Kalibrierschein-Nr./ *Certificate-Nr.* :	Rückführung/ *Traceability* :
020010	47057-PTB-20	PTB
011-2012	47045-PTB-20	PTB

Die Korrektur der spektralen Fehlanpassung (Mismatch), die durch die Abweichung der spektralen Verteilung des Sonnen Simulators vom Standard-Spektrum AM1.5G /3/ in Kombination mit den verschiedenen spektralen Empfindlichkeiten von Referenzzelle und Messobjekt entsteht /4/, wurde durch eine erweiterte Mismatchberechnung /4/ - wie in /2/ beschrieben - korrigiert.

Dazu wurde die spektrale Verteilung der Bestrahlung (Sonnensimulator) mit einem Spektralradiometer und die spektrale Empfindlichkeit des Messobjektes mit einem laserbasierten Messplatz /5/ gemessen (s. Kalibrierschein Nr: 9004087UWW0620).

The spectral mismatch - caused by the deviation of the simulator spectrum from the standard spectrum AM1.5G /3/ in combination with the difference between the spectral response of the reference cell and that of the device under test (DUT) – is calculated by a generalized mismatch correction /3/ as described in /2/.

For the spectral mismatch correction the spectral distribution of the solar simulator is measured with a spectroradiometer, the spectral response of the DUT is measured with a laser-based setup according to /5/ (cf. Calibration Mark: 9004087UWW0620).

Der P_{MPP} wurde durch MPP-Tracking über 300s bestimmt. Der angegebene P_{MPP} ist der Mittelwert von 57-356s dieser stabilisierten Messung. Anschließend wurde die IV-Kennlinie in zwei Richtungen (V_{OC} -> I_{SC} und I_{SC} -> V_{OC}) aufgenommen.

The P_{MPP} was determined by MPP-Tracking for 300s. The reported P_{MPP} represents the average value of the range 57-356s of this stabilized measurement. Afterwards, the IV-curve was determined with a scan in both directions (V_{OC} -> I_{SC} and I_{SC} -> V_{OC}).

Figure S39/2 certificate for J/V scan and stabilized power output

Fraunhofer ISE

10004087UWW0620

CalLab PV Cells

Die Rückführung der Spektralmessung auf SI-Einheiten erfolgte über den Vergleich mit einer Standardlampe.
The traceability of the measurement of the spectral distribution to SI-Units is achieved using a standard lamp for the calibration of the spectroradiometer.

Identitäts-Nr. / *Identity-Nr.* :	Kalibrierschein-Nr./ *Certificate-Nr.* :	Rückführung/ *Traceability* :
BN-9101-451	40006-20-PTB	PTB

3. Messbedingungen

Measurement conditions

Standardtestbedingungen (STC) / *Standard Testing Conditions (STC)* :

Absolute Bestrahlungsstärke / *Total irradiance* :	1000	W/m²
Temperatur des Messobjektes / *Temperature of the DUT* :	25	°C
Spektrale Bestrahlungsstärke / *Spectral irradiance distribution* :	AM1.5G Ed.4 (2019)	

Die Messung der IV-Kennlinie (Strom-Spannungs-Kennlinie) des Messobjektes erfolgt mit Hilfe eines Vierquadranten-Netzteiles und eines Kalibrierwiderstandes.
The measurement of the IV-curve is performed with a 4-quadrant power amplifier and a calibration resistor.

4. Messergebnis

Measurement results

Fläche / *Area* (da)[1]: = (0.0174 ± 0.0011) cm²

[1] : *(t) = total area, (ap) = aperture area, (da) = designated illumination area /7/*

Kennlinienparameter des Messobjektes unter Standardtestbedingungen (STC) / *IV-curve parameter under Standard Testing Conditions (STC)* :

		Vorwärtsrichtung / *forwards scan direction*		Rückwärtsrichtung / *reverse scan direction*		steady state MPP	
V_{oc}	=	(2160 ± 22)	mV	(2163 ± 22)	mV		
I_{SC} (Ed.2 - 2008)	=	(0.2301 ± 0.0048)	mA	(0.2304 ± 0.0048)	mA		
I_{MPP}	=	0.21	mA	0.22	mA	(0.2157 ± 0.0063)	mA
V_{MPP}	=	1867.2	mV	1877.8	mV	(1871 ± 37)	mV
P_{MPP}	=	0.401	mW	0.405	mW	(0.403 ± 0.012)	mW
FF	=	80.64	%	81.25	%		
η	=					(23.1 ± 1.6)	%

Figure S39/3 certificate for J/V scan and stabilized power output

Fraunhofer ISE

CalLab PV Cells

10004087UWW0620

Angegeben ist jeweils die erweiterte Messunsicherheit, die sich aus der Standardmessunsicherheit durch Multiplikation mit dem Faktor *k*=2 ergibt. Sie wurde gemäß dem "Guide to the expression of Uncertainty in Measurement" ermittelt. Sie entspricht bei einer Normalverteilung der Abweichungen vom Messwert einer Überdeckungswahrscheinlichkeit von 95%.
The expanded measurement uncertainty resulting from the standard measurement uncertainty multiplied with a factor k=2 is specified. The calculation was carried out according to the "Guide to the expression of Uncertainty in Measurement". The value corresponds to a Gaussian distribution denoting the deviations of the measurement value within a probability of 95%.

5. Zusatzinformationen
Additional information

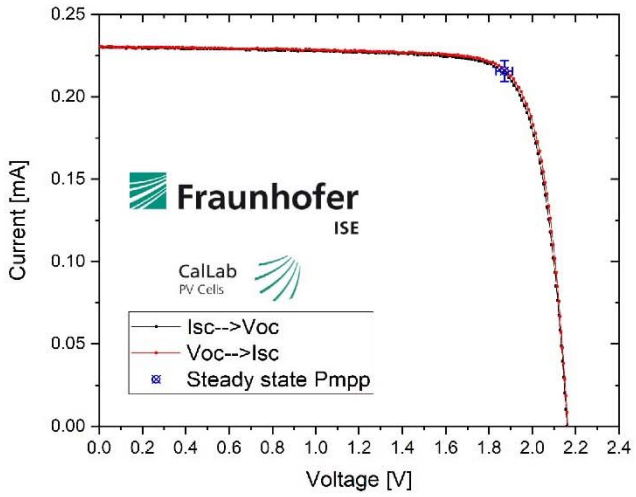

Figure S39/4 certificate for J/V scan and stabilized power output

Fraunhofer ISE

CalLab PV Cells

10004087UWW0620

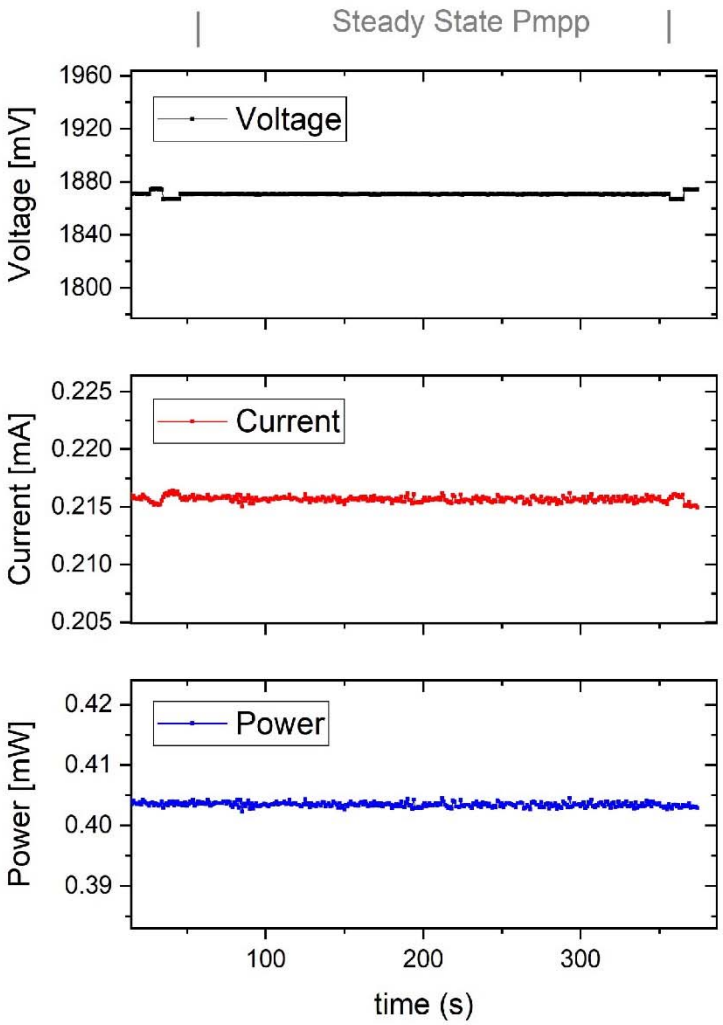

Figure S39/5 certificate for J/V scan and stabilized power output

Fraunhofer ISE

CalLab PV Cells

10004087UWW0620

6.Literatur

Literature

/1/ IEC 60904-1-Ed.3:2020, *Photovoltaic devices - Part 1: Measurement of photovoltaic current-voltage characteristics*

/2/ M. Meusel, R. Adelhelm, F. Dimroth, A.W. Bett, W. Warta Spectral Mismatch Correction and Spectrometric Characterization of Monolithic III–V Multi-junction Solar Cells Prog. Photovolt: Res. Appl. 10 (2002) p. 243–255

/3/ IEC 60904-3-Ed.4:2019, *Photovoltaic devices - Part 3: Measurement principles for terrestrial photovoltaic (PV) solar devices with reference spectral irradiance data*

/4/ IEC 60904-7-Ed.4:2019, *Photovoltaic devices - Part 7: Computation of the spectral mismatch error introduced in the testing of a photovoltaic device*

/5/ IEC 60904-8-Ed.3:2014, *Photovoltaic devices - Part 8: Measurement of the spectral responsivity of a photovoltaic (PV) device*

/6/ IEC 60904-9-Ed.3:2020, *Photovoltaic devices - Part 9: Solar simulator performance requirements*

/7/ M.A. Green, K. Emery, Y. Hishikawa, W. Warta, and E. D. Dunlop, *Solar cell efficiency tables (version 39)*. Progress in Photovoltaics: Research and Applications, 2012. 20: p. 12-20.

Ende des Kalibrierscheins / End of certificate

Figure S39/6 certificate for J/V scan and stabilized power output

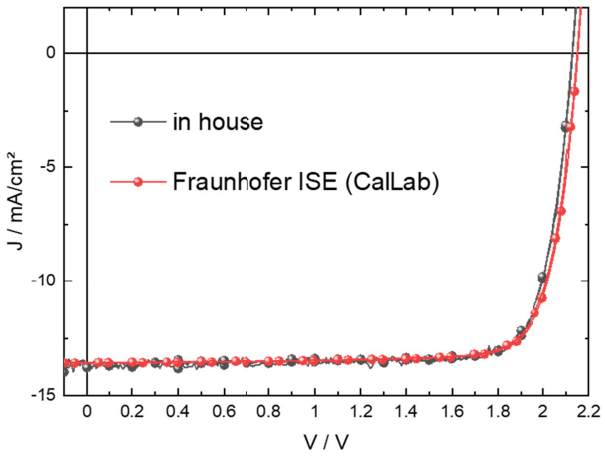

		PCE / %	FF / %	V_{OC} / V	J_{SC} / mA/cm²
in house	reverse	23.8	81	2.13	13.7
	forward	23.7	81	2.13	13.8
Fraunhofer ISE CalLab	reverse	23.8	81	2.15	13.6
	forward	23.6	81	2.15	13.6

Figure S40: Direct comparison of the same tandem cell measured first in our own lab (in house) and then at Fraunhofer ISE CalLab without stress due to a prior EQE measurement (see Supplementary Note 5) using the light source calibration obtained from the certified cell shown in Figure S38 & S39.

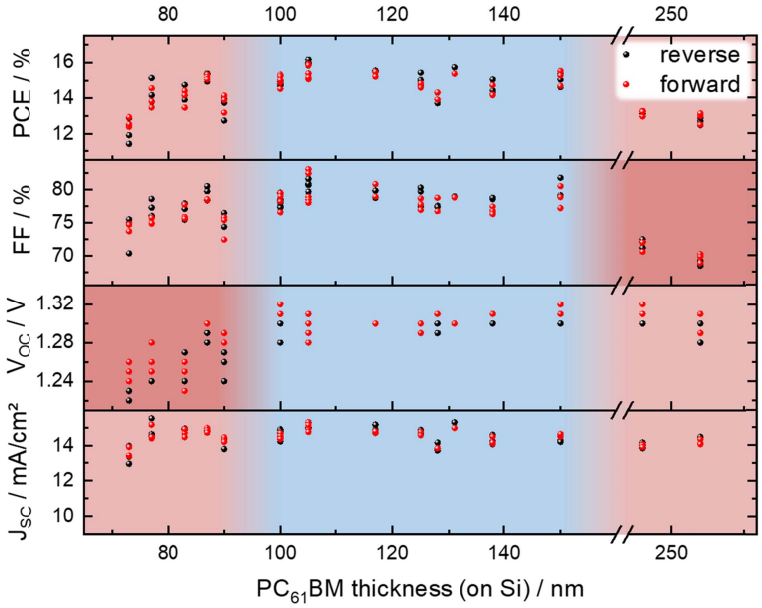

Figure S41: Thickness optimization of the $PC_{61}BM$ layer. The $PC_{61}BM$ thickness was determined by ellipsometry on a silicon reference.

References

1. Brinkmann KO*, et al.* Extremely Robust Gas-Quenching Deposition of Halide Perovskites on Top of Hydrophobic Hole Transport Materials for Inverted (p–i–n) Solar Cells by Targeting the Precursor Wetting Issue. *ACS Applied Materials & Interfaces* **11**, 40172-40179 (2019).

2. Libera JA, Hryn JN, Elam JW. Indium Oxide Atomic Layer Deposition Facilitated by the Synergy between Oxygen and Water. *Chemistry of Materials* **23**, 2150-2158 (2011).

3. Zardetto V, *et al.* Atomic layer deposition for perovskite solar cells: research status, opportunities and challenges. *Sustainable Energy Fuels* **1**, 30-55 (2017).

4. Wei W, Hu YW, Catalytic role of H2O in degradation of inorganic–organic perovskite (CH3NH3PbI3) in air. *Int. J. Energy Res.* **41**, 1063-1069 (2017).

5. Yang J, Siempelkamp BD, Liu D, Kelly LD, Investigation of CH3NH3PbI3 Degradation Rates and Mechanisms in Controlled Humidity Environments Using in Situ Techniques. *ACS Nano* **9**, 1955-1963 (2015).

6. Timmreck R*, et al.* Characterization of tandem organic solar cells. *Nature Photonics* **9**, 478-479 (2015).

7. Zhang S, *et al.* Different Photostability of BiVO4 in Near-pH-Neutral Electrolytes. *ACS Appl. Energy Mater.* **3**, 9523-9527 (2020).

8. Shiga M, *et al.* Sparse modeling of EELS and EDX spectral imaging data by nonnegative matrix factorization. *Ultramicroscopy* **170**, 43-59 (2016)

9. Zhang S, Scheu C, Evaluation of EELS spectrum imaging data by spectral components and factors from multivariate analysis. *Microscopy* **67**, 133-141 (2018).

10. Wurfel P. The chemical potential of radiation. *Journal of Physics C: Solid State Physics* **15**, 3967-3985 (1982).

11. Shockley W, Queisser HJ. Detailed Balance Limit of Efficiency of p-n Junction Solar Cells. *Journal of Applied Physics* **32**, 510-519 (1961).

12. Würfel P, Würfel U. *Physics of Solar Cells: From Basic Principles to Advanced Concepts*. Wiley (2016).

13. Chen C-W, Hsiao S-Y, Chen C-Y, Kang H-W, Huang Z-Y, Lin H-W. Optical properties of organometal halide perovskite thin films and general device structure design rules for perovskite single and tandem solar cells. *Journal of Materials Chemistry A* **3**, 9152-9159 (2015).

14. Sun H*, et al.* A monothiophene unit incorporating both fluoro and ester substitution enabling high-performance donor polymers for non-fullerene solar cells with 16.4% efficiency. *Energy & Environmental Science* **12**, 3328-3337 (2019).

15. Perdigón-Toro L*, et al.* Barrierless Free Charge Generation in the High-Performance PM6:Y6 Bulk Heterojunction Non-Fullerene Solar Cell. *Advanced Materials* **32**, 1906763 (2020).

16. Lin Q, Armin A, Nagiri RCR, Burn PL, Meredith P. Electro-optics of perovskite solar cells. *Nature Photonics* **9**, 106-112 (2015).

17. Rau U, Blank B, Müller TCM, Kirchartz T. Efficiency Potential of Photovoltaic Materials and Devices Unveiled by Detailed-Balance Analysis. *Physical Review Applied* **7**, 044016 (2017).

18. Caprioglio P, *et al.* Nano-emitting Heterostructures Violate Optical Reciprocity and Enable Efficient Photoluminescence in Halide-Segregated Methylammonium-Free Wide Bandgap Perovskites. *ACS Energy Letters* **6**, 419-428 (2021).

19. Belisle RA, *et al.* Impact of Surfaces on Photoinduced Halide Segregation in Mixed-Halide Perovskites. *ACS Energy Letters* **3***,* 2694-2700 (2018).

20. Knight AJ, Herz L. Preventing phase segregation in mixed-halide perovskites: a perspective. *Energy & Enviromental Science* **13**, 2024-2046 (2020).

21. Brinkmann KO*, et al.* Suppressed decomposition of organometal halide perovskites by impermeable electron-extraction layers in inverted solar cells. *Nature Communications* **8**, 13938 (2017).

22. Crowell CR. The Richardson constant for thermionic emission in Schottky barrier diodes. *Solid-State Electronics* **8**, 395-399 (1965).

23. Nagasawa M, Shionoya S, Makishima S. Electron Effective Mass of SnO2. *Journal of the Physical Society of Japan* **20**, 1093-1093 (1965).

24. Werner JH, Güttler HH. Barrier inhomogeneities at Schottky contacts. *Journal of Applied Physics* **69**, 1522-1533 (1991).

25. Chand S, Kumar J. Effects of barrier height distribution on the behavior of a Schottky diode. *Journal of Applied Physics* **82**, 5005-5010 (1997).